Multiphysical modelling of planar solid oxide fuel cell stack layers

N. Russner [a,*], S. Dierickx [a], A. Weber [a], R. Reimert [b], E. Ivers-Tiffée [a]

[a] Institute for Applied Materials (IAM-WET), Karlsruhe Institute of Technology (KIT), D-76131, Karlsruhe, Germany
[b] Engler-Bunte-Institut, Fuel Technology, Karlsruhe Institute of Technology (KIT), D-76131, Karlsruhe, Germany

HIGHLIGHTS

- SOFC modelling by well-defined and complete parameter data set.
- Extensive model validation by temperature tracking and gas conversion measurements.
- Detailed comparison of ASC and ESC cell design.
- Precise quantification of heat sources during SOFC operation.

ARTICLE INFO

Keywords:
Planar SOFC
Cell designs
Stack modelling
Temperature distribution
Heat and mass transport

ABSTRACT

Anode supported (ASC) and electrolyte supported cells (ESC) represent the most common cell concepts in solid oxide fuel cell (SOFC) technology. In ASCs, mechanical manageability is provided by a porous nickel/yttria-stabilized zirconia (Ni/YSZ) substrate, whereas in ESCs a self-supporting dense YSZ electrolyte is applied. Naturally, the electrical loss contributions arising in ASCs and ESCs differ in quantity, leading to different temperature profiles within planar SOFC stacks.

A two-dimensional, finite element method model was developed which considers the underlying chemical and physical processes, and calculates both the electrical performance and the thermal distribution of planar SOFC stack layers operated with reformate fuels. It was then validated by comparing simulation results with extensively measured (i) temperature profiles in SOFC stacks, (ii) gas composition changes along the fuel gas channel of planar ASCs, and (iii) current-voltage characteristics in a temperature range from 650 °C to 800 °C.

The subsequent numerical study reveals (i) the different performances of ASC and ESC, (ii) the impact of operation conditions on performance and temperature profile and (iii) how the individual loss contributions generate temperature distributions in the stack layer.

1. Introduction

Planar stack configurations of solid oxide fuel cells (SOFCs) have attracted much attention in recent years. Compared to tubular stacks, they are simple and affordable to fabricate. Additionally, planar stacks allow the highest power density of all stack configurations, attributed to low in-plane ohmic losses [1,2]. However, the operation of planar SOFC stacks remains challenging. Delamination or crack formation caused by thermomechanical stresses due to an inhomogeneous temperature distribution within the stack have to be especially avoided [1,3,4].

Among self-supporting cell concepts, the most common are anode-supported (ASCs) and electrolyte-supported cells (ESCs), where their mechanical stabilities are provided by the nickel/yttria-stabilized zirconia (Ni/YSZ) substrate and by the YSZ electrolyte, respectively. Due to the low ohmic losses of their thin film electrolyte (approximately 10 µm [5]), ASCs enable operation in a lower temperature range (500–800 °C) [2,6] than for ESCs (850–1000 °C) [5], and also with higher current densities. Despite these ASC advantages, ESCs are still used in a number of SOFC systems on account of their low susceptibility to anode re-oxidation and the strong mechanical support from the solid electrolyte layer [7,8].

The temperature distribution within a SOFC stack results from heat sinks and heat sources, caused by endothermal and exothermal (electro-) catalytic reactions as well as by Joule heating due to ohmic and polarization power losses. These processes strongly depend on the local temperature. When using pre-reformed or even pure hydrocarbon fuel gases, the catalytic reforming of these gases at the nickel surface within the anode [9,10] has also to be dealt with. Consequently, the complex

* Corresponding author.
E-mail address: niklas.russner@kit.edu (N. Russner).

interrelation between local gas composition, temperature and current density distribution, catalytic reactions, charge transfer and the transport of heat, mass and charge must all be considered when describing SOFC stack performance.

Numerous 3D models and simulations have been published, each pursuing different objectives. For example, Achenbach [11] presented the first three dimensional (3D) and nonstationary model of a planar SOFC stack under hydrocarbon fuel operation, evaluating cell efficiency under co-, counter- and crossflow configurations. Studies from Yakabe et al. [3] and from Recknagle et al. [12] focused on the determination of thermal stresses within a stack layer based on simulated temperature profiles. Nishida et al. [13] presented a validated 3D stack model, capable of revealing cell performances depending on their locations within the stack. Anderson et al. [14] analyzed the current density distribution in a 3D stack under H_2/H_2O operation. All these studies provided an important background for further investigation. However, none of the developed models included a detailed description of the electrochemical and catalytic processes based on an experimental model parameterization – only this knowledge would allow a comparison of different cell designs.

The model presented here is based on numerous in-house investigations, frequently published and herein briefly summarized. Electrochemical charge transfer and ohmic charge transport were modeled for stationary and zero dimensional (0D) conditions [15,16], while a unique parameter data set (elaborated by extensive experimental analysis over a broad temperature range and for various cathode and anode gas compositions) provided the model parameters. Microstructural properties of the porous electrodes are determined by parameter setting via focused ion beam/scanning electron microscopy (FIB/SEM) tomography [17,18]. Further applications of this 0D model have been validated for operation with carbon monoxide as fuel gas [19] and for steam electrolysis [20]. Model equations and the parameter data have been implemented into a 2D FEM model, which describes a repeat unit of a planar SOFC stack (RPU). This RPU integrates the electrochemically active cell itself with the metallic interconnector (MIC) (this model approach was published in Ref. [22]). Furthermore, an isothermal 2D FEM model was described in Ref. [23], which calculates gas conversion during hydrocarbon fuel operation along the longitudinal gas flow direction within a SOFC stack layer. Global reaction kinetics for the catalytic steam reforming of methane and the water-gas shift reaction (WGS) [21,22] were integrated in the model. Finally, the model has been extended by including the energy balance on laboratory scale [23].

In this study, our extensive analysis on experimental cells is transferred to stack application by presenting a 2D FEM model of an SOFC stack layer. Thus, SOFC stack operation is described for the first time by an (exclusively) experimentally parameterized model. The model considers occurring loss processes (ohmic and contacting losses, activation and concentration polarization) in every stack layer component and precisely quantifies coupled heat release by appropriate model equations. To determine the temperature distribution, heat transport is considered by reasonable parameter setting for each stack layer component. The spatial resolution of every cell component enables the model to compare different cell designs. By the comparison of ASC and ESC, the impact of cell concept on stack performance and temperature distribution is revealed. Furthermore, the precise quantification of the different heat sources elucidates the physical origin of various temperature profiles.

Simulation results have been extensively validated by measured current-voltage characteristics, fuel gas conversion analysis by gas chromatographic measurements and by temperature tracking along the gas channel on laboratory scale. Furthermore, the model's validity on the stack level is demonstrated by means of stack test results from Forschungszentrum Jülich.

2. Modelling

This study quantitatively analyses the interplay between physical and chemical processes which impact the performance and temperature distribution of a planar SOFC stack layer. The 3D geometry of a single planar anode supported cell (ASC) stack layer is schematically shown in Fig. 1 (a). A FEM model was developed, which accounts for transport of mass, charge and heat, electrochemical charge transfer and catalytic reforming reactions in each cell component. Coupled heat source terms enable a sophisticated attribution of heat release to corresponding loss processes and (electro-) chemical reactions.

Since the computational effort needed to render the complete 3D geometry is immense, gradients perpendicular to the gas flow direction

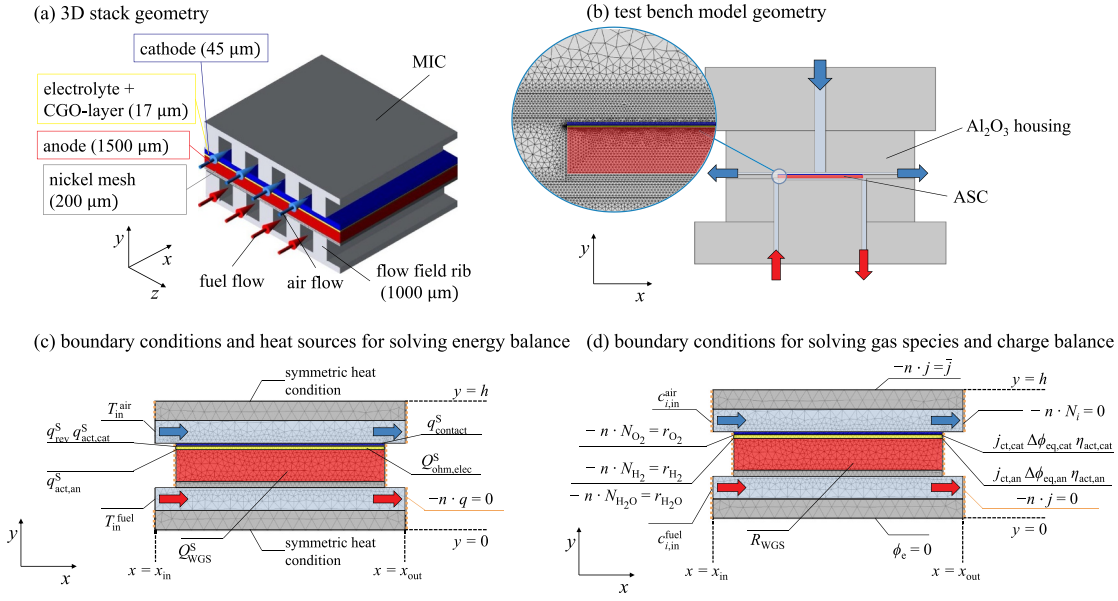

Fig. 1. Schematic of (a) the 3D model geometry of a single planar anode supported cell (ASC) stack layer, (b) the test bench model geometry with numerical mesh, (c) the 2D model geometry with heat sources and boundary conditions with regard to the energy balance equation, and (d) the boundary conditions for species balance for component i on the anode and cathode sides, as well as for the charge balance equation.

Table 1
Overview of governing balance equations.

	equation		model domain
mass balance	$\rho\,\nabla\cdot u \quad 0$	(1)	gas channels/ contact ribs nickel mesh
momentum balance	$\frac{\rho}{\varepsilon}(u\cdot\nabla)\frac{u}{\varepsilon} \quad -\nabla p+\nabla\cdot\left[\frac{\mu}{\varepsilon}(\nabla u+(\nabla u)^T)\right]-\frac{\mu}{\kappa}u$	(2)	gas channels/ contact ribs nickel mesh
charge balance	$\nabla\cdot j \quad 0$	(5)	gas channels/ contact ribs nickel mesh anode electrolyte cathode MIC
species balance	$\nabla\cdot N_i+\nabla\cdot(c_i u) \quad R_{\mathrm{WGS},i}$	(18)	gas channels/ contact ribs nickel mesh anode cathode
energy balance	$\rho\ c_p u\cdot\nabla T+\nabla\cdot q \quad Q^s$	(38)	gas channels/ contact ribs nickel mesh anode cathode electrolyte MIC

(z-direction) are neglected. Thus, the 2D model geometry was homogenized in the area of the flow field ribs and the gas channels. This simplification ignores in-plane diffusion underneath the contact ribs [24], but saves computing times significantly.

The 2D FEM model is described by the governing model equations listed in Table 1.

2.1. Mass and momentum balance

Convective flow, driven by a pressure gradient, mainly contributes to mass transport within the gas channels and the nickel contact mesh. It is described by the continuity equation (mass balance) (Equation (1)) and the Navier-Stokes equation (momentum balance) (Equation (2)), neglecting volume forces. Because of the relatively low flow-velocities, a laminar and incompressible flow of an ideal and Newtonian gas is assumed $\left(\partial\rho/\partial p \quad 0, \rho \quad \frac{p}{RT}\sum x_i M_i\right)$ [25], see Table 1:

$$\rho\nabla\cdot u \quad 0, \tag{1}$$

$$\frac{\rho}{\varepsilon}(u\cdot\nabla)\frac{u}{\varepsilon} \quad -\nabla p+\nabla\cdot\left[\frac{\mu}{\varepsilon}\left(\nabla u+(\nabla u)^{\mathrm{T}}\right)\right]-\frac{\mu}{\kappa}u. \tag{2}$$

For describing the flow in the nickel mesh, momentum balance is extended on the right-hand side, introducing the permeability κ. This and the porosity ε are estimated from the nickel mesh geometry and are denoted in Table 2. Fluid transport properties in this study are determined in dependence of gas composition, pressure and temperature by means of correlations, extracted from Ref. [26].

At the air and fuel gas inlet, mass flow rates are fixed (Equation (3)). The corresponding fluid flow velocity is determined by means of the cross-sectional flow area A:

$$-\int\rho(u\cdot n)dA\Big|_{x\ x_{\mathrm{in}}} \quad m_{\mathrm{in}}. \tag{3}$$

At outlet boundaries, constant pressure is assumed (Equation (4)) ($p_{\mathrm{ref}} \quad 1.013\cdot10^5$ Pa).

$$-pI+\mu\left(\nabla u+(\nabla u)^{\mathrm{T}}\right)\Big|_{x\ x_{\mathrm{out}}} \quad p_{\mathrm{ref}} \tag{4}$$

To ensure a constant ratio between active cell area and gas channel volume after homogenization, half channel height is used in the two-dimensional model.

Table 2
Porosity ε, tortuosity τ and permeability κ for the gas channels, Ni mesh, porous Ni/YSZ anode and LSCF cathode.

	porosity ε	tortuosity τ	permeability κ/m^2	mean pore diameter d_{pore}/ nm
gas channels	1	1	$\to\infty$	–
nickel mesh	0.735	x-direction: 2.2 y-direction: 1	$1.76\cdot10^{-8}$	–
anode substrate	0.415 [18]	3.03 [18]	$1.7\cdot10^{-14}$ [27]	820 [18]
cathode	0.446 [28]	1.92 [28]	$1.27\cdot10^{-15}$ [29]	552 [28]

2.2. Charge balance

Charge conservation is described by Equation (5):

$$\nabla\cdot j \quad 0. \tag{5}$$

The boundary conditions are shown in Fig. 1 (d) and given by Equation (6) at the top, by Equation (7) at the bottom and by Equation (8) at each front side of the 2D geometry, respectively:

$$-n\cdot j|_{y\ \mathrm{h}} \quad \bar{j}, \tag{6}$$

$$\varphi_{\mathrm{e}}|_{y\ 0} \quad 0, \tag{7}$$

$$-n\cdot j|_{x\ x_{\mathrm{in}}} \quad -n\cdot j|_{x\ x_{\mathrm{out}}} \quad 0. \tag{8}$$

In Equations (6)–(8), $\bar{j}$ depicts the average current density, φ_{e} the electronic potential and n the normal vector of the corresponding boundary. The electrical conduction is described by Ohm's law for both electrons and ions:

$$j \quad -\sigma^{\mathrm{eff}}_{\mathrm{e/ion}}\nabla\varphi_{\mathrm{e/ion}}. \tag{9}$$

In Equation (9), φ_{ion} is the ionic potential. The effective electronic conductivities of the electrodes $\sigma^{\mathrm{eff}}_{\mathrm{e}}$ and one condensed ionic conductivity of the electrolyte and the CGO-interlayer $\sigma^{\mathrm{eff}}_{\mathrm{ion}}$ had been experimentally determined over a broad temperature range [19]. Using this condensed conductivity these two layers are treated jointly in one model domain ($d_{8\mathrm{YSZ}} \quad 10$ µm; $d_{\mathrm{CGO}} \quad 7$ µm).

Since the electronic conductivities of the interconnector, the electrodes and the contact mesh are several orders of magnitude higher than the ionic conductivity of the electrolyte, the main part of ohmic loss takes place during ionic transport. The corresponding power loss density, which is equivalent to the generated heat, is quantified by Equation (10):

$$p^{\mathrm{l}}_{\mathrm{ohm,elec}} \quad j\Delta\varphi_{\mathrm{ion}}, \tag{10}$$

where $\Delta\varphi_{\mathrm{ion}}$ denotes the difference of ionic potential between the anode/electrolyte and the cathode/electrolyte interfaces.

For the metallic interconnector, an electronic conductivity value is adopted from Ref. [30] ($\sigma_{\mathrm{MIC}} \quad 4.55\cdot10^6\,\mathrm{S\,m^{-1}}$). Ideal contacting is guaranteed by contact meshes on the cathode and anode sides in the experimental setup; contact resistance between MIC and cathode surface is to be expected in stack layer geometry. Hence, the area specific contact resistance ASR_{contact} is quantified (depending on local temperature T) by means of experimental values, individually determined for the selected flow field geometry and material combination [31]:

$$ASR_{\mathrm{contact}}\Big/\,\Omega\,\mathrm{cm^2} \quad 17119\exp\left(-0.012\frac{T}{\mathrm{K}}\right). \tag{11}$$

2.3. Charge transfer

Charge transfer is assumed to only take place at the electrode/electrolyte interfaces, although in reality there is always a spatial extension of the reaction into the electrode, which is generally described by the penetration depth [32]. As the charge transfer reaction and thus also its penetration depth is highly dependent on the material and microstructural properties of the electrodes and the operating conditions (temperature and gas composition) its value can vary over a wide range. In literature the determined penetration depth within Ni/YSZ cermet anodes spread from 6 to 20 µm [33–35].

In previous studies, it was demonstrated that depending on the temperature the penetration depth within Ni/YSZ cermet anodes varies between 10 µm at 950 °C and 14 µm at 750 °C (x_{H_2O} 0.05) [36] and for the LSCF cathode between 2.3 and 10 µm in the temperature range between 600 and 900 °C [37]. However, the individual electrode thicknesses are much larger than the expected penetrations depths. Hence, the impact of the penetration depth on the performance prediction is assumed to be negligible.

The charge transfer current density $j_{ct,el}$ is determined for each electrode by the well-established Butler-Volmer equation [38]:

$$j_{ct,el} \quad j_{0,el}\left[\exp\left(\alpha_{el}\frac{n_e F\eta_{act,el}}{RT}\right)-\exp\left(-(1-\alpha_{el})\frac{n_e F\eta_{act,el}}{RT}\right)\right], \tag{12}$$

where α_{el} denotes the charge transfer coefficient, n_e the number of transferred electrons, F the Faraday constant, R the ideal gas constant and T the local temperature. As demonstrated [39–41], we assume that by supplying a reformate fuel mixture, only hydrogen is directly electrochemically converted, whereas CO is only converted by the water-gas shift reaction. Thus, the exchange current densities $j_{0,el}$ are specified for the anode and cathode sides as follows:

$$j_{0,an} \quad \gamma_{an}\left(\frac{p_{H_2,an/elec}}{p_{ref}}\right)^{a}\left(\frac{p_{H_2O,an/elec}}{p_{ref}}\right)^{b}\exp\left(-\frac{E_{act,an}}{RT}\right), \tag{13}$$

$$j_{0,cat} \quad \gamma_{cat}\left(\frac{p_{O_2,cat/elec}}{p_{ref}}\right)^{m}\exp\left(-\frac{E_{act,cat}}{RT}\right). \tag{14}$$

In Equations (13) and (14), the temperature dependency of $j_{0,el}$ is defined by pre-factors γ_{el} and the activation energies $E_{act,el}$. By reaction orders *a, b* and *m,* charge transfer kinetics are expressed depending on the local partial pressure p_i of each involved species. Please note that every model parameter in Equations (12) - (14) is experimentally determined by electrochemical impedance spectroscopy (EIS) [19]. The capability of this parameter dataset to precisely predict cell performance over a broad range of operating parameters (including SOEC) was proven in Refs. [20,24].

The activation overpotentials $\eta_{act,el}$ are modeled by potential balancing at the individual electrode/electrolyte interface in dependency to local electronic and ionic potential $\varphi_{e,ion}$ and half-cell potentials $\Delta\varphi_{eq,el}$:

$$\eta_{act,an} \quad \varphi_e-\varphi_{ion}-\Delta\varphi_{eq,an}\left(p_{i,an/elec}\right), \tag{15}$$

$$\eta_{act,cat} \quad -\varphi_e+\varphi_{ion}+\Delta\varphi_{eq,cat}\left(p_{i,cat/elec}\right). \tag{16}$$

For a detailed derivation of Equations (15) and (16) the reader is referred to Ref. [24]. The power losses at each electrode, $P^{l}_{act,el}$ (which originate from passing of the electrochemical double layer), are determined by Equation (17):

$$P^{l}_{act,el} \quad j_{ct,el}\,\eta_{act,el}. \tag{17}$$

2.4. Species balance

For operation with pre-reformed fuels the balance equation (18) is solved for H_2, H_2O, CO, CO_2 and N_2 on the fuel gas side and for O_2 and N_2 on the air side, respectively:

$$\nabla\cdot N_i+\nabla\cdot(c_i u) \quad R_{WGS,i}. \tag{18}$$

The left-hand side of Equation (18) comprises diffusion and convection. Fuel and air are assumed to enter the model domain at a fixed composition:

$$c_i|_{x\ x_{in}} \quad x_{i,in}\frac{p}{RT}. \tag{19}$$

In Equation (19), $x_{i,in}$ depicts the mole fraction of component *i* at the inlet. Molar density is calculated via ideal gas law. At outlet boundaries, no diffusive flux is assumed (Fig. 1 (d)):

$$-n\cdot N_i|_{x\ x_{out}} \quad 0. \tag{20}$$

Gas composition changes due to the electrochemical conversion of oxygen on the air side:

$$O_2+4e \rightleftharpoons 2O^2, \tag{21}$$

and due to oxidation of hydrogen on the fuel side:

$$2H_2+2O^2 \rightleftharpoons 2H_2O+4e. \tag{22}$$

Electrochemical reactions are assumed to only occur at the electrode/electrolyte interfaces. There, the area specific reaction rate r_i is coupled to the current density, $j_{ct,cat}$ and $j_{ct,an}$, via the Faraday constant F and an electron balance, derived from Equation (21) and Equation (22), respectively. Thus, area specific reaction rate is set at cathode/electrolyte interface:

$$-n\cdot N_{O_2}|_{cat/elec} \quad r_{O_2} \quad \frac{j_{ct,cat}}{4F}, \tag{23}$$

and analogously at anode/electrolyte interface:

$$-n\cdot N_{H_2}|_{an/elec} \quad r_{H_2} \quad \frac{j_{ct,an}}{2F}, \tag{24}$$

$$-n\cdot N_{H_2O}|_{an/elec} \quad r_{H_2O} \quad \frac{j_{ct,an}}{2F}. \tag{25}$$

The kinetics of diffusive species transport within the gas channels and the contact mesh are implemented by Maxwell-Stefan equations [42]:

$$\sum_{\substack{j\\ j/i}}^{n}\frac{x_jN_i-x_iN_j}{\frac{p}{RT}\frac{\varepsilon}{\tau}D_{ij}} \quad -\nabla x_i-(x_i-\omega_i)\frac{\nabla p}{p}. \tag{26}$$

In Equation (26), ω_i depicts the mass fraction of component *i*. The porosity ε and the tortuosity τ of the respective model domain are listed in Table 2.

Binary diffusion coefficients D_{ij} are determined by the Chapman-Enskog relation [43]:

$$D_{ij} \quad 1.868\cdot10^{-7}\frac{m^2}{s}\cdot\frac{\left(T/K\right)^{1.5}\sqrt{\left(\frac{M_i}{10^{-3}kg\ mol^{-1}}\right)^{-1}+\left(\frac{M_j}{10^{-3}kg\ mol^{-1}}\right)^{-1}}}{\frac{p}{p_{ref}}\left(\frac{\sigma_{ij}}{10^{-10}m}\right)^{2}\Omega_{ij}}. \tag{27}$$

In Equation (27), M_i denotes the molar mass of component *i*, σ_{ij} the average collision diameter and Ω_{ij} the collision integral of the components *i* and *j*.

Due to the comparable length scale of pore diameter and the mean free path length in the porous SOFC electrodes (Knudsen number between 0.3 and 0.7), both intermolecular diffusion and Knudsen diffusion had to be taken into account for an appropriate mass transport kinetic

approach. This was achieved by the well-established Dusty-Gas model [44], which covers the gas species balance and momentum balance by abstracting the porous medium as giant, uniformly distributed molecules. The Dusty-Gas model is implemented in the form suggested by Zhu et al. [45]:

$$\sum_{\substack{j\\ j/i}}^{n} \frac{c_j N_i - c_i N_j}{\frac{p}{RT}\frac{\varepsilon}{\tau}D_{ij}} + \frac{N_i}{\frac{\varepsilon}{\tau}D_{\mathrm{Kn},i}} \quad -\nabla c_i - \frac{c_i}{\frac{\varepsilon}{\tau}D_{\mathrm{Kn},i}}\frac{\kappa}{\eta}\nabla p. \tag{28}$$

The Knudsen-diffusion coefficient of species i, $D_{\mathrm{Kn},i}$, is calculated according to Equation (29) [44].

$$D_{\mathrm{Kn},i} \quad \frac{1}{3} d_{\mathrm{pore}} \sqrt{\frac{8RT}{\pi M_i}}. \tag{29}$$

An explicit representation of N_i within the porous electrodes can be derived from Equation (28) [45].

$$N_i \quad -\sum_{j}^{n} D_{ij}^{\mathrm{DGM}} \nabla c_j - \left(\sum_{j}^{n} D_{ij}^{\mathrm{DGM}} \frac{c_j}{\frac{\varepsilon}{\tau}D_{\mathrm{Kn},j}} \right) \frac{\kappa}{\eta}\nabla p. \tag{30}$$

In Equation (30), D_{ij}^{DGM} depicts the DGM diffusion coefficients, which can be represented by an inverse of matrix H:

$$D_{ij}^{\mathrm{DGM}} \quad H^{-1}. \tag{31}$$

The elements of H, h_{ij}, are described by Equation (32).

$$h_{ij} \quad \left(\frac{1}{\frac{\varepsilon}{\tau}D_{\mathrm{Kn},i}} + \sum_{\substack{k\\ k/i}}^{n} \frac{x_k}{\frac{\varepsilon}{\tau}D_{ik}} \right) \delta_{ij} + \frac{x_i}{\frac{\varepsilon}{\tau}D_{ij}} (\delta_{ij} - 1), \tag{32}$$

where δ_{ij} denotes the Kronecker delta. Our group already published the required microstructural parameters of the porous electrodes, e.g. porosity ε, tortuosity τ, permeability κ and mean pore diameter d_{pore} (highly relevant for gas transport in porous media). These were determined by high-resolution FIB/SEM tomography [18,28] and are listed in Table 2.

Under reformate fuel operation, gas mixture components are converted via the catalytic activated WGS in the anode. Hence, the reaction rate of WGS, R_{WGS}, appears in the individual gas species balance according to the stoichiometric coefficients:

$$\mathrm{CO} + \mathrm{H_2O} \rightleftharpoons \mathrm{H_2} + \mathrm{CO_2} \qquad \Delta H_{\mathrm{R}}^{0} \quad -41.2\,\mathrm{kJ/mol}. \tag{33}$$

It is very often assumed that the WGS is at local equilibrium [3,11,46–48]. However, Kromp et al. [39] showed an influence of WGS kinetics on the polarization resistance comparing the impedance spectra of Ni/8YSZ anodes under reformate fuel operation and hydrogen operation. In the presented model, the kinetics of the catalytic WGS are implemented by the volumetric reaction rate in the anode model domain R_{WGS}, whereby homogeneous gas phase reactions are neglected [49]. Its kinetic is determined by means of a global reaction rate, proposed in Ref. [50]:

$$R_{\mathrm{WGS}} \quad k_{\mathrm{WGS}} \left(p_{\mathrm{CO}}\, p_{\mathrm{H_2O}} - \frac{1}{K_{eq,\mathrm{WGS}}} p_{\mathrm{CO_2}}\, p_{\mathrm{H_2}} \right). \tag{34}$$

Equation (34) reflects forward and reverse WGS. The corresponding reaction rate constants are related by the equilibrium coefficient $K_{\mathrm{eq,WGS}}$, which is calculated (dependent on local temperature) using the thermodynamic database MALT ® [51]:

$$K_{eq,\mathrm{WGS}} \quad \exp\left(-4.235 + \frac{4521\ \mathrm{K}}{T} \right) + 0.0999. \tag{35}$$

Reaction rate constant for the forward WGS k_{WGS} is determined by fitting an Arrhenius approach to experimental data:

$$k_{\mathrm{WGS}} \quad A_{\mathrm{WGS}} \cdot \exp\left(-\frac{E_{\mathrm{act,WGS}}}{RT} \right), \tag{36}$$

where A_{WGS} denotes the pre-exponential factor and $E_{\mathrm{act,WGS}}$ the activation energy of WGS. These parameters were individually set for the used test cells by analyzing fuel gas conversion along the gas channel. This analysis was carried out on the test bench, which will be introduced in Section 3.1. By fitting the Arrhenius approach to the experimental results in the operating temperature range of 650–800 °C, the parameters were determined to A_{WGS} 0.027 mol $\mathrm{Pa^{-2}\ m^{-3}\ s^{-1}}$ and $E_{\mathrm{act,WGS}}$ 83.73 kJ $\mathrm{mol^{-1}}$. Reaction rate constant for 800 °C according to Equation (36) is one order of magnitude higher than the value reported by Lehnert in Ref. [50]. However, in view of high uncertainty of kinetic data for the WGS reaction in SOFC anodes in literature, this value is still within reasonable range.

Anodic concentration overpotential is defined by means of a modified Nernst equation [19] based on the partial pressures of hydrogen and steam, which are important in the gas channel (GC) and at the anode/electrolyte interface (an/elec), respectively. By multiplying the concentration overpotential with the charge transfer current density on the anode side $j_{\mathrm{ct,an}}$, the corresponding power loss density $p_{\mathrm{conc,an}}^{\mathrm{l}}$ is evaluated:

$$p_{\mathrm{conc,an}}^{\mathrm{l}} \quad \frac{RT}{2F} \ln \left(\frac{p_{\mathrm{H_2O,an/elec}}\, p_{\mathrm{H_2,GC}}}{p_{\mathrm{H_2O,GC}}\, p_{\mathrm{H_2,an/elec}}} \right) j_{ct,an}. \tag{37}$$

2.5. Energy balance

For spatially resolved determinations of temperature profile, the energy balance is implemented in the model framework:

$$\rho c_p u \cdot \nabla T + \nabla \cdot q \quad Q^{\mathrm{s}}. \tag{38}$$

Simulations are performed assuming fixed gas inlet temperatures:

$$T|_{x\ x_{\mathrm{in}}} \quad T_{\mathrm{in}}, \tag{39}$$

and adiabatic boundary condition at the outlets and at the front sides of the stack:

$$-n \cdot q|_{x\ x_{out}} \quad 0. \tag{40}$$

To account for the thermal interaction between the adjacent stack layers, a symmetry heat condition is set at top surface (y h) and bottom surface (y 0) of the model domain:

$$-n \cdot q|_{y\ h} \quad n \cdot q|_{y\ 0}. \tag{41}$$

Heat conduction vector q and convective heat transport, consisting of the density ρ, the specific heat capacity c_p and the fluid flow velocity vector u are denoted on left-hand side of the energy balance (Equation (38)). Convective heat transport is solely considered in the gas channels and in the contact mesh, while it is assumed that heat is transported only by conduction in the solid components of the geometry. The influence of surface-to-surface radiative heat transfer across the gas channels (y-direction) was found to be negligible, based on an estimation which considers the flow field and cell surfaces to be black bodies [52]. In the theoretical case of black bodies, the maximum amount of heat is transported via radiation. Due to the small-scale channel height and the high thermal conductivity of the interconnector material (see Table 3), less than 2.5% of heat is transported by black-body radiation. Concerning radiative heat transfer along the flow gas direction (x-direction), small view factors of solid surfaces lead to a negligible radiation contribution. Conductive heat transport is modeled by Fourier's law [53]:

$$q \quad \frac{Q}{A_{\perp}} \quad -k \nabla T. \tag{42}$$

Table 3
Average thermal conductivities of solid stack components (valid for T = 500–1000 °C).

Solid material phase	Thermal conductivity k/W m ^{1} K ^{1}
MIC (Crofer 22 APU) [30]	24
Ni [56]	90.7
Au [26]	317
8YSZ [57]	2
LSCF [58]	3.2
Al_2O_3 [59]	8.773 – 3.3·10 ^{3} T/K

In Equation (42), q is defined by the heat conduction vector Q per unit area normal to heat flux direction $A_{\perp}$. Heat transport properties of the porous electrodes and the contact mesh are reflected by effective thermal conductivities k^{eff}. These effective thermal conductivities are composed by the conductivity of solid phase k_{solid} which is listed in Table 3 and the conductivity of fluid phase k_{fluid} [26]. Effective thermal conductivity for nickel contact mesh $k^{\text{eff}}_{\text{mesh}}$ is specified as:

$$k^{\text{eff}}_{\text{mesh}} \quad k_{\text{solid}}(1-\varepsilon_{\text{mesh}}) + k_{\text{fluid}}\varepsilon_{\text{mesh}}. \tag{43}$$

The effective heat conductivities of the Ni/YSZ anode and the LSCF cathode were determined by heat transport simulations in the 3D porous microstructure. Thereby, heat conduction within reconstructed microstructures was taken into account individually for each material phase by means of the thermal conductivities of the bulk phases [18,28]. A temperature difference between opposite boundaries was set as model parameter. The solution of this problem is a spaced-resolved heat conduction vector. The effective thermal conductivities of the porous media were evaluated using the dimensions of the model domain, the averaged heat conduction vector and the temperature difference [29]. A comparison of these effective conductivities against analytical correlations from literature revealed that the Effective Medium Theory (EMT) [54] showed excellent consistency for the Ni/YSZ anode and LSCF cathode. According to EMT, the effective thermal conductivity can be expressed as:

$$k^{\text{eff}}_{\text{el}} \quad \begin{array}{c} 0.25\left[(3\varepsilon_{\text{el}}-1)k_{\text{fluid}} + (3(1-\varepsilon_{\text{el}})-1)k_{\text{solid}}\right] \\ +0.25\sqrt{\left[(3\varepsilon_{\text{el}}-1)k_{\text{fluid}} + (3(1-\varepsilon_{\text{el}})-1)k_{\text{solid}}\right]^2 + 8k_{\text{fluid}}k_{\text{solid}}} \end{array}. \tag{44}$$

The solid-phase thermal conductivity of the Ni/YSZ cermet anode is also determined by EMT [55].

In the homogenized model domains, heat is transported by convection in the gas channels and by conduction in the contact ribs. Since a significant part of the heat is transported in both components, corresponding transport equations are assigned to the identical model domains, particularly since heat flux direction differs in both transport paths. Thus, while in the real stack geometry half of the cell surface is in physical contact with the contact ribs and the gas channel respectively, in the 2D model it is assumed that the cell is completely surrounded both with the channel and with the contact ribs. In regards to heat conduction in y-direction, the cross sectional area normal to the heat flux is doubled $\left(A_{\perp\text{hom}} \quad 2A_{\perp,\text{ini}}\right)$. As described in Section 2.1, channel height is halved $(\text{d}y_{\text{hom}} \quad 0.5\text{d}y_{\text{ini}})$ in terms of fluid flow modelling due to the homogenization. As the heat flux in y-direction does not change due to homogenization ($Q_{\text{hom,y}} \quad Q_{\text{ini,y}}$), the thermal conductivity in y-direction in the homogenized domains is determined with Equation (42):

$$-k_{\text{hom}}\frac{\text{d}T}{0.5\text{d}y_{\text{ini}}}2A_{\perp,\text{ini}} \quad -k_{\text{ini}}\frac{\text{d}T}{\text{d}y_{\text{ini}}}A_{\perp,\text{ini}}\ . \tag{45}$$

Thus, thermal conductivities in y-direction in the homogenized domains were multiplied by a factor of 0.25:

$$k_{\text{hom}} \quad \begin{pmatrix} k_{\text{ini}} & 0 \\ 0 & 0.25\ k_{\text{ini}} \end{pmatrix} \tag{46}$$

Heat generation due to electrochemical losses and (electro-) chemical reactions is implemented by appropriated heat source terms. Thereby, volumetric heat sources Q^{s} appear explicitly in Equation (38), while area specific heat sources are implemented as internal boundary conditions, denoted in Equation (47) for general model domains l and m:

$$k_l\frac{\text{d}T}{\text{d}n}\bigg|_l - k_m\frac{\text{d}T}{\text{d}n}\bigg|_m \quad q^{\text{s}}. \tag{47}$$

In the following, heat sources terms are listed and discussed in detail. Fig. 1 (c) depicts all heat sources in regard to their spatial location.

The main part of heat is released due to the electrochemical conversion at the electrode/electrolyte interfaces, and can be calculated by entropy balancing [60]. Although the overall reaction is strongly exothermic, heat is released by the electrochemical reduction of oxygen at cathode/electrolyte interface (Equation (21)) and consumed by the electrochemical oxidation of hydrogen (Equation (22)) at the anode/electrolyte interface under standard SOFC operating conditions. Considering the electrode reactions, described by Equations (21) and (22), the molar entropies of the oxygen ions and electrons are unknown. Thus, attribution of generated heat to electro-oxidation and -reduction can only be estimated by experimental investigations [61]. However, corresponding data is rare in literature and not given for the gas compositions and temperatures that are of interest. Since the dependency on gas composition at these interfaces should be investigated, entropy transfer of the overall electrochemical reaction is considered in the model:

$$q^{\text{s}}_{\text{rev}} \quad -T\left(2S_{\text{H}_2\text{O,an/elec}} - 2S_{\text{H}_2\text{,an/elec}} - S_{\text{O}_2\text{,cat/elec}}\right)\frac{j_{\text{ct,cat}}}{4F}. \tag{48}$$

Because the main part of heat is released by the electrochemical reduction of oxygen (Equation (21)) [62], q^{s}_{rev} is attributed to the cathode/electrolyte interface. The molar entropies of the involved gas species S_i are specified by Equation (49), assuming air and fuel as ideal gases [63]:

$$S_i \quad S_i^0\left(T_{\text{ref}},\ p_{\text{ref}}\right) + c_{p,i}\,M_i\,\ln\left(\frac{T}{T_{\text{ref}}}\right) - R\ln\ \frac{p_i}{p_{\text{ref}}}\ . \tag{49}$$

Therein, S_i^0 depicts the molar entropy under standard conditions (T_{ref} 298.15 K, p_{ref} $1.013\cdot10^5$ Pa), $c_{p,i}$ the specific heat, M_i the molar mass and p_i the partial pressure of species i. Thus, heat generation due to the electrochemical conversion is expressed by Equations (48) and (49) depended on local temperature and gas species concentration. From the latter dependency it follows that heat sources due to gas diffusion polarization are indirectly considered by the resulting gas composition at electrode/electrolyte interfaces, i.e. the entropy change related to the gas diffusion.

Irreversibilities accompanied with charge transfer are assumed to generate heat quantitatively. Thus, heat source $q^{\text{s}}_{\text{act,el}}$ is specified by activation power loss density (Equation (17)) on electrode/electrolyte interfaces:

$$q^{\text{s}}_{\text{act,el}} \quad p^{\text{l}}_{\text{act,el}}. \tag{50}$$

In the anode substrate, slightly exothermic WGS acts as a heat source and is quantified by reaction rate R_{WGS} and the molar reaction enthalpy $\Delta_{\text{R}}H_{\text{WGS}}$:

$$Q^{\text{s}}_{\text{WGS}} \quad -R_{\text{WGS}}\ \Delta_{\text{R}}H_{\text{WGS}}. \tag{51}$$

The reaction enthalpy of WGS is calculated depending on local temperature by thermodynamic data extracted from MALT ® [51]:

$$\Delta_{\text{R}}H_{\text{WGS}}\Big/\text{kJ mol}^{-1} \quad 0.0094\cdot\frac{T}{\text{K}} - 44.326. \tag{52}$$

Joule heating during charge transport is only considered for ionic conduction in the electrolyte:

$$Q^{\text{s}}_{\text{ohm,elec}} \quad \frac{j^2_{\text{ion}}}{\sigma^{\text{eff}}_{\text{ion}}}. \tag{53}$$

Table 4
Inlet gas flows and fuel gas compositions for validation measurements.

	dieselATR [69]	H_2 operation (single cell)	stack operation (a) ($\bar{j}$ 0.5 A cm ^{2})	stack operation (b) ($\bar{j}$ 0.41 A cm ^{2})
$V_{in}^{fuel}\left(p_{ref}, T_{ref}\right)$ /m^3 s ^{1}	1.273 · 10 ^{5}	0.833 · 10 ^{5}	52.167 · 10 ^{5}	52.328 · 10 ^{5}
$V_{in}^{air}\left(p_{ref}, T_{ref}\right)$ /m^3 s ^{1}	1.107 · 10 ^{5}	1.667 · 10 ^{5}	268.333 · 10 ^{5}	255.257 · 10 ^{5}
$u_{in}^{fuel}\left(p_{ref}, T_{in}\right)$ /m s ^{1}	2.63	1.72	1.12	1.13
$u_{in}^{air}\left(p_{ref}, T_{in}\right)$ /m s ^{1}	1.72	2.60	5.46	5.24
H_2	0.23	0.49	0.9	0.9
H_2O	0.24	0.01	0.1	0.1
CO	0.13	–	–	–
CO_2	0.03	–	–	–
N_2	0.37	0.5	–	–

Heat source due to contact resistance is implemented via area specific contact resistance $ASR_{contact}$ at interconnector/cathode interface:

$$q^{s}_{contact} \quad j\, ASR_{contact}. \tag{54}$$

2.6. Model adaption on laboratory geometry

Since the presented 2D FEM model accounts for numerous coupled physical and chemical processes in the SOFC, a validation requires various experiments (i.e. local gas conversion, temperature measurements and current-voltage characteristics). Some of these are hard to perform in a stack. Thus, we adapted the presented model to a sophisticated test bench for single cell measurements [22] and solved the set of equations with the finite element method. A schematic of this test bench is shown in Fig. 1 (b). As denoted in Fig. 1 (b) air flow is supplied by an impinging jet, while fuel gas flows along the active cell area.

The adapted model considers heat transport in the chemically inert Al_2O_3 (alumina) housing. The corresponding thermal conductivity is depicted in Table 3. Only heat radiation (Equation (55)) is considered between housing and furnace atmosphere:

$$q_{rad} \quad \varepsilon_{rad}\sigma_{rad}\left(T^4 - T_O^4\right). \tag{55}$$

In Equation (55), ε_{rad} denotes the emissivity of Al_2O_3 which is set to 0.3 [64], σ_{rad} the Stefan-Boltzmann constant and T_O the furnace temperature. Fuel and air are assumed to enter the model domain at furnace temperature. The Au mesh is added in the model geometry. Corresponding parameters can be found in Tables 2 and 3 The contact resistances of cathode/Au mesh and Ni/YSZ anode/Ni mesh were determined to be below 5 and 2 mΩ cm^2 respectively [65]; thus the contact resistances on both electrodes can be neglected in the laboratory geometry.

3. Test units for validation

3.1. Single cell

The SOFC test cells analyzed in this study are state-of-the-art ASCs with Ni/YSZ cermet anode, 8YSZ electrolyte, $Ce_{0.8}Gd_{0.2}O_{2-\delta}$ (CGO) interlayer and a mixed electron and ion conducting $La_{0.58}Sr_{0.4}Co_{0.2}Fe_{0.8}O_{3-\delta}$ (LSCF) cathode manufactured by Forschungszentrum Jülich [2,66,67]. Corresponding layer thicknesses are denoted in Fig. 1 (a).

For single cell tests, these cells are inserted into an Al_2O_3 housing (Fig. 1 (b)). Gas flow rates are adjusted by digital mass flow controllers (MFCs). A gas mixing battery enables a variation of inlet fuel compositions with up to five components. Fuel gas compositions and corresponding flow rates are denoted in Table 4. The entire housing is installed in an oven, which allows the furnace temperature to be varied independently of operating conditions. In order to monitor the temperature profile along the cell, three thermocouples are installed in the ceramic housing at 3, 20 and 37 mm from fuel inlet (x-direction) and 7 mm under the Ni contact mesh (y-direction). For *in situ* fuel conversion analysis, five small Al_2O_3 tubes were installed at equal distances along the anode flow field, through which fuel gases could be extracted and analyzed with a Micro-gas-chromatograph (Varian CP4900). Ideal contacting is ensured by an Au mesh on the cathode side and a Ni mesh on the anode side. Further information about the test setup is provided in Ref. [22].

3.2. Stack

The model is validated with experimental data from an 18-layer stack of ASCs manufactured and operated by Forschungszentrum Jülich. The Jülich F-design stack consists of an MIC with lateral dimensions of 317 × 224 mm, made from ferritic chromium steel by ThyssenKrupp (Crofer 22 APU), and ASCs with the same cell chemistry and layer thicknesses as described above. The ASC has an active cell area A_{cell} of 190 x 190 mm^2. A nickel mesh for anode contacting was integrated between the interconnector and anode substrate. Seven thermocouples were inserted 10 mm deep into the MIC plate of an inner layer at different positions along the gas channel. For model validation we consider two different current densities under supply of air as oxidant and 10% humidified hydrogen as fuel (Table 4). Operation results of the stack used for model validation in this study were published in Ref. [68].

4. Validation

4.1. Single cell

4.1.1. Temperature distribution - Fig. 2 (a)

The measured and simulated housing temperatures agree very well, and are almost identical to furnace temperature under open circuit voltage (OCV) conditions ($\bar{j}$ 0 A cm^{-2}). The temperatures rise with increasing current density up to 764 °C, at current density of 1 A cm^{-2}. The model over-estimates this temperature increase by up to 20%. The strongest deviation is noticeable at the highest current density of 1 A cm^{-2}. The measured temperature is almost constant along the cell, but the simulation results in a parabolic profile (with maximum temperature in the center). Besides the simplified 2D model geometry, an important cause for this deviation is that the complex thermal interactions between the housing surface and furnace cannot be accurately reproduced by the radiation kinetics (Equation (55)).

The temperature gradient perpendicular to cell plane increases with the averaged current density, indicated by the temperature difference between the anode/electrolyte interface and the thermocouple location. Overall, the capability of the model to reflect thermal distribution in the single cell setup could be clearly demonstrated for different current densities.

4.1.2. Fuel gas composition profile - Fig. 2 (b)

Due to the small channel height, any concentration gradient in y-direction within the gas channels can be neglected, and simulation results for half fuel-channel height (lines) were used for validation. The

total agreement between simulation and experimental values along gas flow direction (x-direction) excellently validates the modelling of viscous fluid flow by Equations (1) and (2), of species transport by Equations (26) and (28) and of catalytic reforming kinetics by Equation (34).

In the first section (0–20 mm from gas inlet) the concentration profile seems to indicate that the WGS reaction (Equation (31)) compensated the electrochemical hydrogen oxidation. In the section of 20–40 mm from gas inlet, ongoing electrochemical oxidation (implemented by Equations (24) and (25)) causes the hydrogen concentration to decrease and the steam concentration to increase. The monotonous decrease of the CO mole fraction results from the pervasive WGS reaction (Equation (33)).

In Fig. 2 (b), the simulated mole fraction profiles at the anode/electrolyte interface are shown in dashed lines. Due to the smaller molar weight of hydrogen (H_2) compared to steam (H_2O), hydrogen diffuses much faster, resulting in an approximately smaller-by-half concentration gradient perpendicular to the cell plane ($\overline{\partial x_{H_2}/\partial y}$ 31.1 m^{-1}; $\overline{\partial x_{H_2O}/\partial y}$ – 59.4 m^{-1}). In contrast to H_2/H_2O, CO and CO_2 are not converted at the anode/electrolyte interface, but actually within the entire anode substrate. Hence, the concentration gradients of these two species are relatively small.

4.1.3. *Current-voltage characteristics - Fig. 2(c) and (d)*

Experimental data were available for varying furnace temperatures (650–800 °C) and for two fuel gases: (i) dieselATR and (ii) 1% humidified mixture of hydrogen (H_2) and nitrogen (N_2) (Table 4).

The comparison of measured and simulated CV-curves is shown in Fig. 2 (c) and (d). The model is able to reflect the temperature dependence of OCV for both fuel gas compositions. For dieselATR as fuel (Fig. 2 (c)), cell voltage decreases linearly with average current densities below 1 A cm^{-2} for furnace temperatures of 750 °C and 800 °C. Ohmic losses are predominant for these elevated operating temperatures and high fuel humidity, while activation polarization is negligible [15]. For current densities above 1 A cm^{-2} a non-linear decrease of cell voltage is noticeable, attributable to diffusion losses in the anode substrate. This steep gradient is more visible for furnace temperature T_O 800 °C than for T_O 750 °C, and it is reflected by the model. Under $H_2/N_2/H_2O$ operation (Fig. 2 (d)), a steep voltage loss under low current densities is present, especially at furnace temperature $T_O \leq 700$ °C. This voltage drop is attributable to polarization [15] caused by electrochemical charge transfer. The good agreement between measurement and simulation results indicates an excellent display of activation losses via Butler-Volmer approach (Equation (12)) and the included parameters.

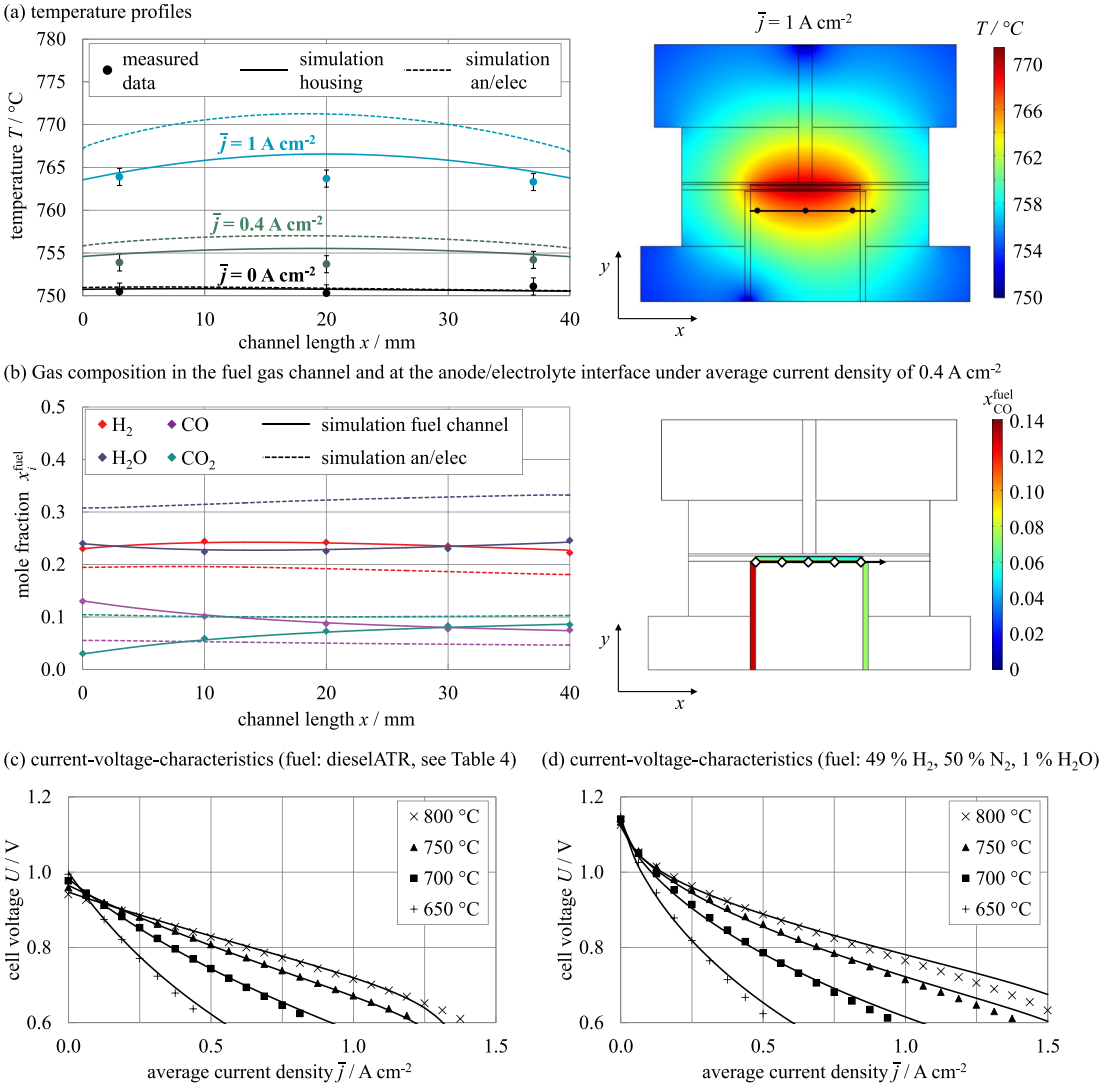

Fig. 2. Comparison of simulation results (lines) and measured data (symbols) after at least 1-h operation. Furnace temperature $T_O = 750$ °C; fuel gas flow rate 1.273 · 10 ^{5} m^3 s^{-1} (dieselATR, Table 4, standard condition); air as oxidant with a gas flow of 1.107 · 10 ^{5} m^3 s^{-1} (standard condition).

4.2. Stack layer

The applicability of the FEM model on stack geometries was proven by means of stack tests, performed by Forschungszentrum Jülich [68] on an 18-layer stack of ASCs. The stack was operated with air as oxidant and 10% humidified hydrogen as fuel in counter flow configuration and with an average current density of 0.5 A cm^{-2} and 0.41 A cm^{-2}, respectively (see Table 4). The temperature profiles shown in Fig. 3 and cell voltage were measured in (and calculated for) the middle layer of the stack.

Gas flow within the feed tubes is not considered by the model. Hence, gas inlet temperatures are not predictable and were set in the simulation to the outer temperature probes. These temperature probes are located outside of the active cell area.

The model qualitatively reflects the temperature profiles very well for both considered operating conditions, indicated by mean absolute error along the MIC length of 9.5 K for average current density of 0.5 A cm^{-2} (9.0 K for 0.41 A cm^{-2}). However, around the maximum temperature under average current density of 0.5 A cm^{-2}, the difference between measured and simulated MIC temperature is approximately 18 K, which corresponds to 21% of the temperature increase relative to furnace temperature (ΔT 85 K). This deviation is attributable to the simplified 2D model geometry.

Cell voltage U and resulting power output P (Table inside Fig. 3) are very precisely redacted. Given the good correspondence for most properties in experiment and simulation, one can confidently regard the model as valid.

5. Simulation results and discussion

5.1. Power loss densities

The local distribution of the power loss densities p^{l} (Equation (10), (17) and (37)) characterize the performance of an SOFC. For the single cell test setup, the power loss densities and the influences of (i) the furnace temperature T_O and (ii) the average current densities $\bar{j}$ on them were calculated and revealed by simulations. Inlet gas compositions were set to dieselATR as fuel and air as oxidant (flow rates shown Table 4).

The courses of the power loss densities over the channel length, shown in Fig. 4, clearly indicate a strongly varying temperature dependency of the loss mechanisms. At T_O 850 °C (Fig. 4 (a) and (d)), concentration polarization is decisive, expressed by the highest power loss density along the entire active cell area. Concentration polarization shows a negligible temperature dependency, while the activation overpotentials of the electrodes show a moderate dependency, and the ohmic loss strongly rises with decreasing temperature. Even for the thin electrolyte (d_{elec} $d_{8YSZ} + d_{CGO}$ 17 µm), ohmic loss dominates for intermediate and low operating temperatures of 750 and 650 °C. Regarding temperature influence on the activation polarization power losses $p^{l}_{act,el}$, the higher activation energy for the cathode ($E_{act,cat}$) compared to the anode ($E_{act,an}$) [24] leads to there being a slightly steeper increase of power loss density with decreased temperature.

The increase of the average current density from 0.4 to 1 A cm^{-2} at the same temperature reveals a significant increase of total power loss, whereas the relative contribution of the individual losses remains approximately constant. This behavior is related to the cell design and the operating conditions. Neither the diffusion limitation current density nor a limiting fuel utilization are reached at any point along the gas channel.

5.2. Comparison of ASC and ESC stack layer arrangements

In the previous section, power losses during SOFC operation were calculated in dependency of operating conditions. In the following

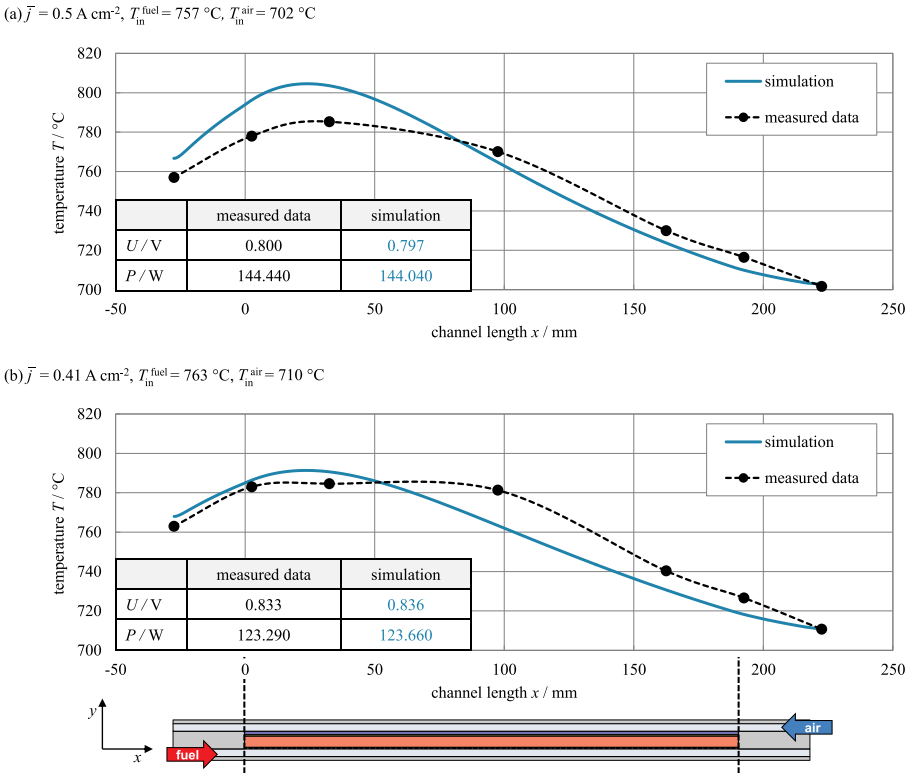

Fig. 3. Comparison of simulated (line) and measured (symbols) temperature profiles in the MIC of an ASC stack layer. The stack is operated with 10% humidified hydrogen as fuel and air as oxidant. Furnace temperature is 700 °C. Simulated and measured cell voltage and power output under the average current density of (a) 0.5 A cm^{2} and (b) 0.41 A cm^{2} are tabled directly in the diagram.

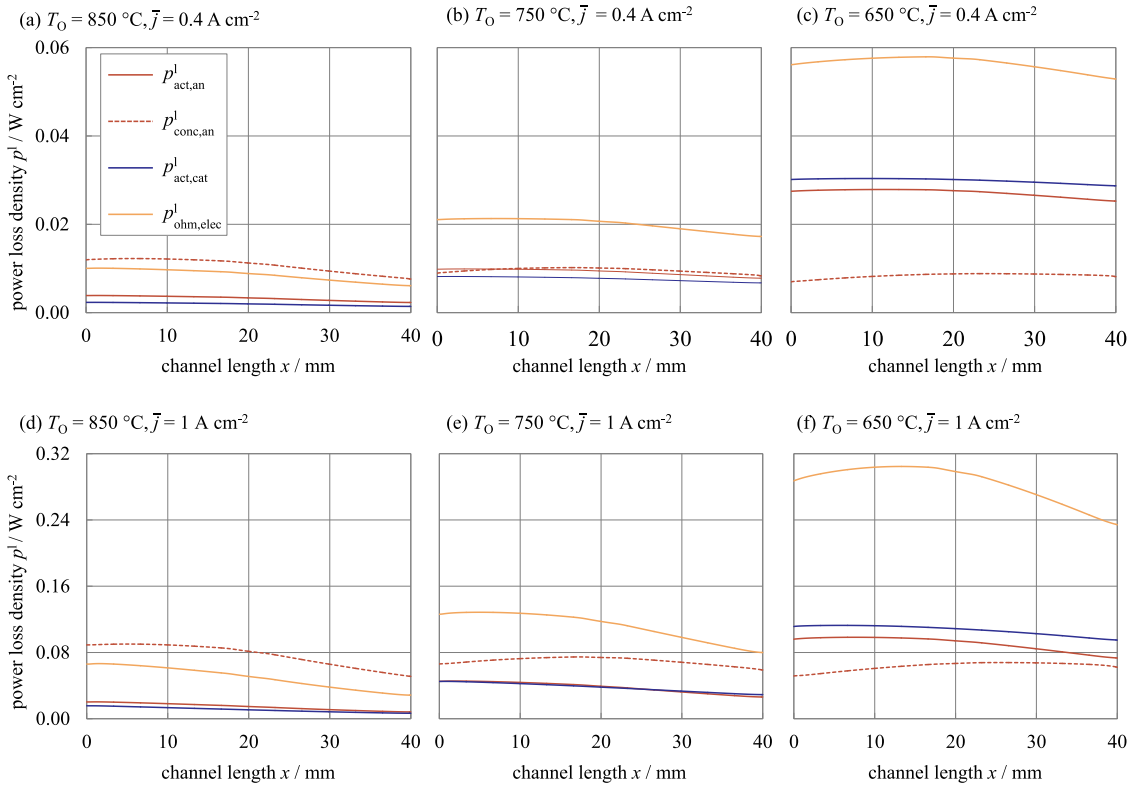

Fig. 4. Power loss densities in single anode supported test cell with active cell area of 16 cm^2.

section these losses, their attributed heat generations and their consequences for performance data are discussed for both ASC and ESC cell configurations. For an unbiased investigation, it is assumed that ESC and ASC differ solely in layer thicknesses and exhibit the same microstructural and material properties. The layer thicknesses of electrodes and electrolytes are given in Table 5.

Simulations were conducted with dieselATR as fuel (see Table 4) and air as oxidant. For describing operation conditions, common key figures like fuel utilization u_{fuel} (Equation (56)), and air-fuel ratio Λ_{air} (Equation (57)), are used throughout the following. Both quantities relate the electrochemically converted fuel/air amount $(\bar{j}\,A_{cell})$ to the supplied fuel/air amount $\left(V_{in}\sum n_e c_{i,in}\right)$.

Simulation results in terms of stack layer performance are displayed by electrical cell efficiency η_{el} (Equation (58)), which relates the electrical power output P to the chemical energy of the fuel. The latter is determined by the fuel volume flow rate V_{in}^{fuel} and the lower heating value of the fuel LHV. Temperature profiles are compared by temperature increase ΔT (Equation (59)), which denotes the difference between maximum and gas inlet temperature. In order to compare volumetric and area-specific heat sources (Equation (48), (50), (51), (53) and (54)) the total amount of released heat is evaluated by integration over volume or area, respectively. The integral heat sources $\overline{Q}^s$, are calculated by Equations (60) and (61). All parameters are defined in Table 6.

Simulation results for a variation of the gas inlet temperature T_{in} between 650 and 950 °C are shown in Fig. 5 for ASC and ESC. The course

Table 5
Layer thicknesses of anode supported cell (ASC) and electrolyte supported cell (ESC).

	ASC	ESC
$d_{sub,an}$/µm	1500	45
d_{elec}/µm	17	150
d_{cat}/µm	45	45

Table 6
List of parameters for characterization of operating conditions, predicted performance and temperature profile by the model.

parameter	description		unit	equation
fuel utilization u_{fuel}	u_{fuel}	$\dfrac{\bar{j}\,A_{cell}}{V_{in}^{fuel}\left(2\,c^{fuel}_{H_2,\,in}+\,2\,c^{fuel}_{CO,\,in}\right)}$	–	(56)
air-fuel ratio Λ_{air}	Λ_{air}	$\dfrac{V_{in}^{air} 2\,c^{air}_{O_2,in}}{\bar{j}\,A_{cell}}$	–	(57)
electrical cell efficiency η_{el}	η_{el}	$\dfrac{P}{V_{in}^{fuel}\,LHV}$	–	(58)
temperature increase ΔT	ΔT	$T_{max}-T_{in}$	K	(59)
integral heat sources $\overline{Q}^s$	$\overline{Q}^s_V$	$\iiint Q^s dx\ dy\ dz$	W	(60)
	$\overline{Q}^s_A$	$\iint q^s\ dx\ dz$	W	(61)

of cell efficiency over gas inlet temperature (Fig. 5 (a)) reveals a constant higher performance of ASC as compared to ESC, until a gas inlet temperature of 950 °C when nearly the same power outputs are generated by both ASC and ESC.

However, the gas inlet temperature influences the electrical efficiency of the two stack layer configurations quite differently. While the ASC stack layer obtains a maximum power output of 113 W at approximately T_{in} 800 °C, the efficiency of the ESC increases monotonously with gas inlet temperature.

Cell efficiencies increase in the temperature range of 650–800 °C for both cell designs. In the gas inlet temperature range of 800–950 °C, the contribution of diffusion polarization increases slightly, which lowers ASC cell efficiency. In the diagram (Fig. 5 (a)) the corresponding operating cell voltage U is denoted as the secondary y-axis. For the ESC, cell voltage is less than 0.6 V for gas inlet temperatures below 800 °C.

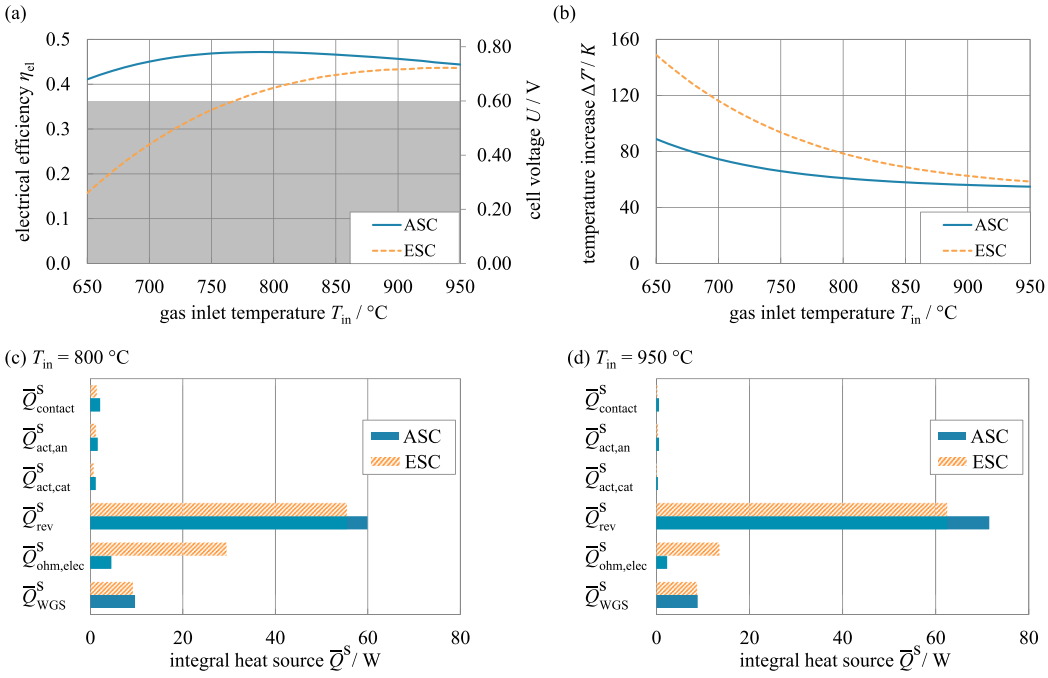

Fig. 5. Simulation results for anode supported (ASC) and for electrolyte supported (ESC) stack layers (fuel: dieselATR; fuel utilization: $u_{fuel} = 0.8$; oxidant: air; air-fuel ratio: $\Lambda_{air} = 4$ in co-flow configuration; average current density $\bar{j} = 0.4$ A cm ^{2}).

Besides low power output, electrochemical nickel re-oxidation is a risk at such a low cell voltage [70].

The temperature increases ΔT in the stack layers (Fig. 5 (b)) inversely follows the electrical efficiency trends (Fig. 5 (a)) with respect to amount and distinction between ASC and ESC. A detailed look at the quantities of the integral heat sources due to the individual power losses

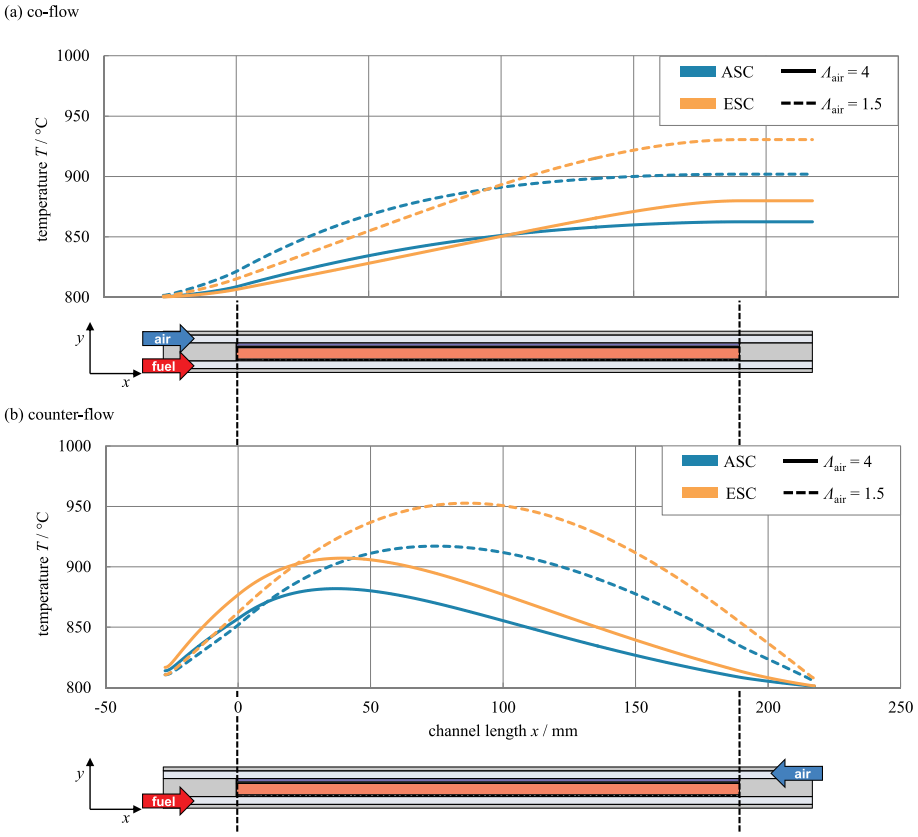

Fig. 6. Simulated temperature profiles along the gas channels within the interconnector for anode supported (ASC) and electrolyte supported (ESC) stack layers (gas inlet temperature: $T_{in} = 800$ °C; fuel: dieselATR; fuel utilization: $u_{fuel} = 0.8$; oxidant: air; average current density $\bar{j} = 0.4$ A cm ^{2}).

(Fig. 5 (c) and (d)) explains the trends and the differences between ESC and ASC. The main distinction originates from Joule heating in the electrolyte. Due to the thinner electrolyte in ASC (Table 5), Joule heating is significantly reduced compared to the ESC (Fig. 5 (c)). With increasing operating temperature, the ohmic loss process is diminished by the rising ionic conductivity of 8YSZ, which causes the courses of ΔT for the ASC and the ESC to converge.

A further difference between ASC and ESC is visible in the amount of reversible heat $\overline{Q}^{S}_{rev}$. A relatively low hydrogen concentration and high steam concentration at the anode/electrolyte interface results from limiting gas transport kinetics in the anode substrate of the ASC. According to Equation (48), entropy transfer (and thereby heat release by the electrochemical conversion) increases with decreased partial pressure of hydrogen and increased steam content. Thus, more heat is released by the electrochemical conversion within the ASC. This effect is more pronounced for T_{in} 950 °C, since the reversible heat release rises with the temperature.

5.3. Comparison of co- and counter-flow

Co- and counter-flow of air relative to fuel gas strongly influence the exit temperatures of air and exhaust gas as well as the temperature distribution within the gas channel. For ASC and ESC cell designs, this influence was studied for two air-fuel ratios Λ_{air} (4 and 1.5, respectively). Other operating conditions were kept constant: average current density was set to 0.4 A cm^{-2}, fuel gas conversion to 0.8 and gas inlet temperature to 800 °C.

Simulation results are shown in Fig. 6 (a) for co-flow and in Fig. 6 (b) for counter-flow. ASC and ESC cell designs result in qualitatively similar temperature profiles. In the first section of the ASC stack layer (0–100 mm), the temperature is slightly higher than in the ESC layer under co-flow operation. The temperature profiles intersect in the stack layer center (Fig. 6 (a)). Diffusion polarization and gas conversion limit the electrochemical charge transfer (Equation (13)) in the region near the fuel outlet of the ASC layer. Hence, a more inhomogeneous current density distribution is present in the ASC than in the ESC layer, with its maximum near the fuel inlet (0.67 A cm^{-2} under Λ_{air} 4). However, a higher maximum temperature is obtained from the ESC stack layer. As discussed above, the higher temperature increase is due to higher heat release by Joule heating in the ESC. Thus, the application of ASCs enables the reduction of cooling air.

Co-flow exhibits a monotonous temperature increase while the counter-flow temperature rises to a maximum. Cell efficiencies are roughly two to five percent (relative) higher for counter-flow (Table 7). Reducing the air-fuel ratio from 4 to 1.5 leads to an increase of ΔT in the range of 35–50 K for the regarded cell concepts and flow configurations. Under counter-flow operation, the maximum temperature shifts from the region surrounding the fuel inlet to the center of the stack layer. The presented results clearly show that co-flow operation is advantageous in terms of reducing thermal gradients within a stack layer.

5.4. Variation of fuel utilization

According to its definition in Equation (56) fuel utilization u_{fuel} can be adjusted by the average current density and/or by the fuel gas flow and composition. For the simulation results shown in Fig. 7 the fuel gas and its flow rate were fixed and average current density was altered. By changing the average current density the power output of the stack layer changes accordingly.

Table 7
Predicted electrical cell efficiency η_{el} for simulations shown in Fig. 6.

	η_{el}, ASC		η_{el}, ESC	
Λ_{air}	co-flow	counter-flow	co-flow	counter-flow
4	0.47	0.48	0.39	0.41
1.5	0.45	0.47	0.41	0.43

Fig. 7 (a) and (b) show that for ESC the electrical efficiency η_{el} and the temperature increase ΔT linearly increase with fuel utilization over the fuel utilization range of 0.7–0.95. Meanwhile, ASC shows the same behavior for low fuel utilization, until a maximum cell efficiency is reached at u_{fuel} 0.92. For fuel utilization higher than 0.92, the ASC cell efficiency decreases and the maximum temperature increases non-linearly.

In the fuel utilization range of 0.7–0.9, the increase of load current dominates the slight voltage loss due to activation and concentration polarization and ohmic losses. Consequently, power output P and cell efficiency η_{el} increase in this fuel utilization range for both cell designs.

To explain the differing behaviors of ASC and ESC in the fuel utilizations range above 0.92, 2D profiles of the partial pressure of hydrogen p_{H_2} were calculated and are shown in Fig. 7 (c)–(f) for ASC and ESC at fuel utilizations of 0.7 and 0.95, respectively. For the lower fuel utilization, the hydrogen concentration profile along the fuel gas flow direction is nearly the same for both cell configurations. For a high fuel utilization of 0.95 (Fig. 7 (d) and (f)), the concentration gradient along the gas channel (x-direction) is reasonably steeper for both the ESC and the ASC. However, a steep gradient is generated within the anode substrate of ASC (y-direction). This gradient leads to an inhomogeneous hydrogen profile at the anode/electrolyte interface of the ASC, which causes the decrease of electrical efficiency.

In Fig. 7 (g) and (h), integral heat sources are compared for ASC and ESC. The heat release due to electrochemical conversion $\overline{Q}^{S}_{rev}$ is approximately the same in both cell designs at u_{fuel} 0.7 but is much higher for ASC at a fuel utilization of 0.95. As discussed above, more heat is generated by the electrochemical reaction under low hydrogen concentration (Equation (48)). Consequently, hydrogen depletion (due to high gas conversion and high diffusion losses) indirectly influences thermal distribution within the ASC stack layer at extremely high fuel utilization.

The presented results clearly show that the electrochemical losses of ESCs are dominated by ohmic resistance of the electrolyte. Therefore, optimization can be achieved by thinner electrolyte layers and/or materials with higher ionic conductivities. On the other hand, the power output of ASC is limited by diffusion losses within the anode substrate, particularly in high fuel utilization range. Since diffusion losses decrease with decreased temperature (Fig. 5), ASC application enables SOFC operation at lower temperatures. Our study shows that the optimization of gas transport on fuel side would lead to higher power output and simultaneously lower temperature gradients within the stack.

6. Conclusions

A 2D FEM model was presented, which calculates both the electrical performance and the thermal distribution of planar solid oxide fuel cell (SOFC) stack layers. It necessarily follows that transport equations for heat, fluid flow and multi-component gas transport are coupled with equations for catalytic reforming kinetics, electrical conduction, electrochemical charge transfer reactions and associated heat sources. All model parameters have been experimentally determined using appropriate test benches and samples. The excellent validity of the 2D FEM model has been proven, experimental data were assessed without free parameter fit. All relevant sub-processes necessary for quantifying electrical loss and associated heat sources were taken into consideration and attributed to their physical origins.

The model was validated using experimental data on anode supported cells and planar SOFC stacks:

- Correctness of simulated temperature distribution was proven by temperature profiles measured (i) on 16 cm^2 ASCs and (ii) on one planar 18-layer SOFC stack.

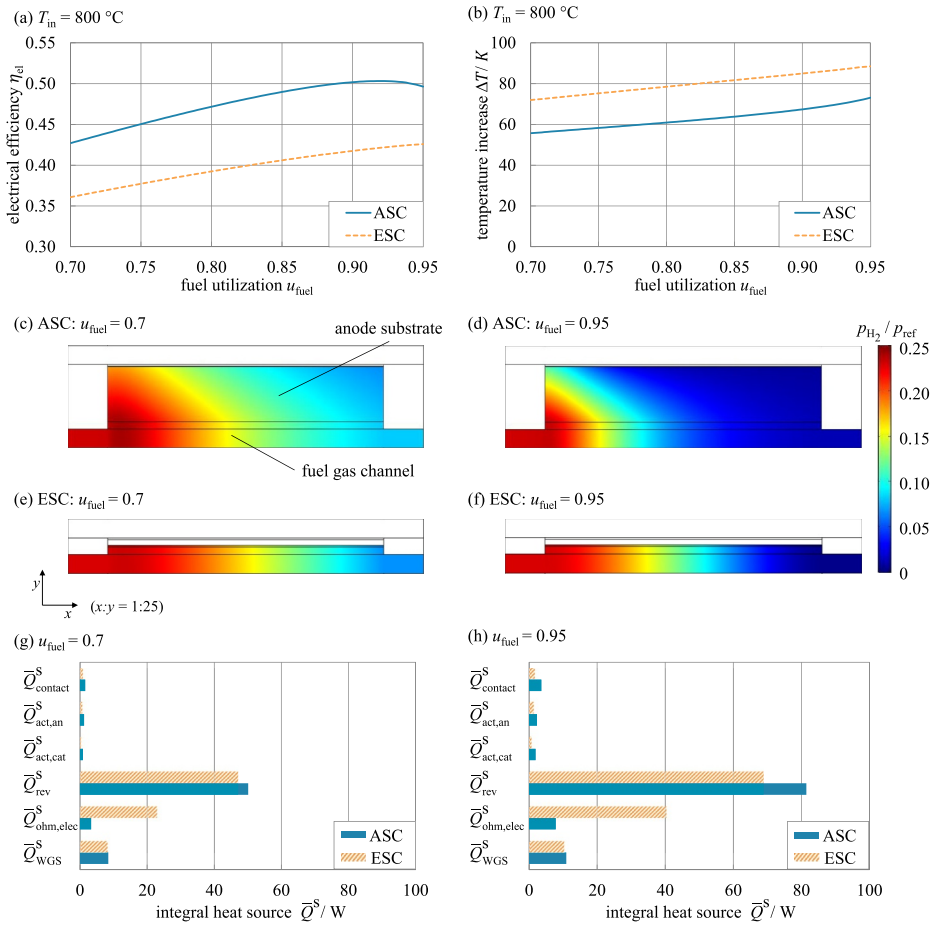

Fig. 7. Simulated performance results for anode supported (ASC) and for electrolyte supported (ESC) stack layers for a variation of fuel utilization, u_{fuel} (gas inlet temperature: T_{in} = 800 °C; fuel: dieselATR; oxidant: air; air-fuel ratio: Λ_{air} = 4, co-flow). Figures on top show (a) electrical cell efficiency η_{el} and (b) temperature increase ΔT within the stack geometry. For fuel utilizations of 0.7 and 0.95, respectively, pictures and graphs show distribution of hydrogen on the fuel side ((c)–(f)), as well as integral heat sources ((g)–(h)).

- Correctness of implemented (electro)chemical kinetics was proven by gas conversion measurements at five positions along the fuel gas channel, via gas chromatography.
- Correctness of simulated current-voltage characteristics was proven by comparison with measured current-voltage characteristics at different temperatures (650–800 °C).

The unique strengths of the presented 2D FEM model were proven by simulation and quantitative performance comparison of anode supported (ASC) with electrolyte supported (ESC) stack layers with dieselATR as fuel in co-flow and counter-flow configuration:

- The ohmic loss contribution within ESC stack layers is solely responsible for a lower power output with simultaneously higher temperature increase within a gas inlet temperature range of 650–950 °C.
- For ASC and ESC stack layers, co-flow-operation leads to a smaller temperature gradient compared to counter-flow-operation. At gas inlet temperature of 800 °C and fuel utilization of 0.8, the temperature increase for the ASC is 20 K higher for counter-flow configuration compared to co-flow configuration.
- For ASC stack layers, cooling air can be saved compared to ESC. At a gas inlet temperature of 800 °C and fuel utilization of 0.8, the maximum temperature within an ASC layer is only 22 K higher than in an ESC layer, if the air-flow rate is reduced by a factor of 2.7.
- In ASC stack layers the efficiency drops, generating a steep temperature gradient at fuel utilizations above 0.92, which is caused by a depletion of hydrogen at the anode/electrolyte interface.

It should be noted, that the 2D FEM model is also applicable for many other SOFC cell materials, cell designs and stack geometries. It is well-suited for extended parameter studies and thus identifies the “ideal” operating window for each design option.

The presented study is an important basis for future work as it provides the detailed modelling of reaction and transport kinetics and corresponding effects on performance and temperature profile of one stack layer. This sophisticated modelling approach will be further homogenized to enable the simulation of an entire 3D SOFC stack with reasonable computational effort.

Declaration of competing interest

The authors declare that they have no known competing financial interests or personal relationships that could have appeared to influence the work reported in this paper.

Acknowledgments

The authors gratefully acknowledge funding from the Bundesministerium für Wirtschaft und Energie (BMWi 03ETB005E and 03ET6056E). Sincere thanks are given to J. Packham for proofreading the manuscript.

Nomenclature

$A_{\perp}$	unit area normal to the direction of heat flux
A_{WGS}	pre-exponential factor (mol Pa^{-2} m^{-3} s^{-1})
A_{cell}	active cell area (m^2)
a,b,m	reaction order in Butler-Volmer approach
ASR_{concact}	area specific contact resistance (Ω m^{-2})
B	empirical coefficient in Chapman-Enskog approach (m^4 $\mathrm{kg}^{0.5}$ s^{-1} $\mathrm{K}^{-1.5}$ $\mathrm{mol}^{-0.5}$)
c_i	molar concentration of species i (mol m^{-3})
c_p	specific heat (J kg^{-1} K^{-1})
d	thickness, diameter (m)
E_{act}	activation energy (J mol^{-1})
F	Faraday constant (C mol^{-1})
$\Delta_{\mathrm{R}}H$	enthalpy of reaction (J mol^{-1})
I	unit matrix
j	current density (A m^{-2})
$\bar{j}$	average current density (A m^{-2})
j_0	exchange current density (A m^{-2})
k	thermal conductivity (W m^{-1} K^{-1})
K_{eq}	equilibrium coefficient
k_{WGS}	reaction rate constant of water-gas shift reaction (mol Pa^{-2} m^{-3} s^{-1})
LHV	lower heating value (J m^{-3})
M_i	molar weight of component i (kg mol^{-1})
n	normal vector
n_{e}	number of transferred electrons
N	molar flux density (mol m^{-2} s^{-1})
p	pressure (Pa)
P	electrical power output (W)
p^{l}	power loss density (W m^{-2})
q	heat flux density (W m^{-2})
Q	heat flux vector (W)
q^{s}	area specific heat source (W m^{-2})
Q^{s}	volumetric heat source (W m^{-3})
$\overline{Q}^{\mathrm{s}}$	integral heat source (W)
r	area specific reaction rate (mol m^{-2} s^{-1})
R	universal gas constant (J mol^{-1} K^{-1})
R_{WGS}	global reaction rate of water-gas reaction (mol m^{-3} s^{-1})
S_i	molar entropy of component i (J mol^{-1} K^{-1})
u	fluid velocity vector (m s^{-1})
U	voltage (V)
u_{fuel}	fuel utilization
T	temperature (K)
V	volume flow rate (m^3 s^{-1})
x, y, z	Cartesian coordinates

Greek letters

α	charge transfer coefficient
γ	pre-exponential factor in Butler-Volmer equation (A m^{-2})
ε	porosity
$\varepsilon_{\mathrm{rad}}$	emissivity
η	overvoltage (V)
η_{el}	electrical efficiency
κ	permeability (m^2)
μ	dynamic viscosity (kg m^{-1} s^{-1})
Λ_{air}	air-fuel ratio
ρ	density (kg m^{-3})
σ	electrical conductivity (S m^{-1})
σ_{ij}	the average collision diameter of gas species i and j (m)
σ_{rad}	Stefan-Boltzmann constant (W m^{-2} K^{-4})
τ	tortuosity
φ	electrical potential (V)
$\Delta\ \varphi_{\mathrm{eq}}$	half-cell potential (V)
Ω_{ij}	the collision integral of gas species i and j

Subscripts

0	standard conditions
A	area specific
act	activation
an	anode
cat	cathode
conc	concentration
ct	charge transfer
e	electronic
eff	effective
el	electrode
elec	electrolyte
fluid	fluid phase
GC	gas channel
hom	homogenized
i	gas species i
in	inlet
ini	initial
ion	ionic
O	furnace
ohm	ohmic
out	outlet
rad	radiation
rev	reversible
ref	reference
solid	solid phase
sub	substrate
V	volumetric

Abbreviations

ASC	anode supported cell
ATR	autothermal reforming
CGO	$Ce_{0.8}Gd_{0.2}O_{2-\delta}$
DRT	distribution of relaxation times
ESC	electrolyte supported cell
EMT	effective medium theory
FEM	finite element method
FIB/SEM	focused ion beam/scanning electron microscopy
LSCF	$La_{0.58}Sr_{0.4}Co_{0.2}Fe_{0.8}O_{3-\delta}$
MFC	mass flow controller
MIC	metallic interconnector
OCV	open circuit voltage
WGS	water-gas shift reaction
YSZ	Yttria-stabilized zirconia

References

[1] S.C. Singhal, K. Kendall, High Temperature and Solid Oxide Fuel Cells, Elsevier, 2003, https://doi.org/10.1016/B978-1-85617-387-2.X5016-8.

[2] N.H. Menzler, F. Tietz, S. Uhlenbruck, H.P. Buchkremer, D. Stover, Materials and manufacturing technologies for solid oxide fuel cells, J. Mater. Sci. 45 (2010) 3109–3135, https://doi.org/10.1007/s10853-010-4279-9.

[3] H. Yakabe, T. Ogiwara, M. Hishinuma, I. Yasuda, 3-D model calculation for planar SOFC, J. Power Sources 102 (2001) 144–154, https://doi.org/10.1016/S0378-7753(01)00792-3.

[4] L. Blum, S.M. Groß, J. Malzbender, U. Pabst, M. Peksen, R. Peters, I.C. Vinke, Investigation of solid oxide fuel cell sealing behavior under stack relevant conditions at Forschungszentrum Jülich, J. Power Sources 196 (2011) 7175–7181, https://doi.org/10.1016/j.jpowsour.2010.09.041.

[5] L. Blum, W.A. Meulenberg, H. Nabielek, R. Steinberger-Wilckens, Worldwide SOFC technology Overview and benchmark, Int. J. Appl. Ceram. Technol. 2 (2005) 482–492, https://doi.org/10.1111/j.1744-7402.2005.02049.x.

[6] N.Q. Minh, Solid oxide fuel cell technology - features and applications, Solid State Ion. 174 (2004) 271–277, https://doi.org/10.1016/j.ssi.2004.07.042.

[7] F. Fleischhauer, R. Bermejo, R. Danzer, A. Mai, T. Graule, J. Kuebler, Strength of an electrolyte supported solid oxide fuel cell, J. Power Sources 297 (2015) 158–167, https://doi.org/10.1016/j.jpowsour.2015.07.075.

[8] T. Strohbach, F. Mittmann, C. Walter, D. Schimanke, C. Geipel, Sunfire industrial SOC stacks and modules, ECS Trans 68 (2015) 125–129, https://doi.org/10.1149/06801.0125ecst.

[9] J.R. Rostrup-Nielsen, J.B. Hansen, S. Helveg, N. Christiansen, A.-K. Jannasch, Sites for catalysis and electrochemistry in solid oxide fuel cell (SOFC) anode, Appl. Phys. A 85 (2006) 427–430, https://doi.org/10.1007/s00339-006-3702-1.

[10] A. Kromp, H. Geisler, A. Weber, E. Ivers-Tiffée, Electrochemical impedance modeling of gas transport and reforming kinetics in reformate fueled solid oxide fuel cell anodes, Electrochim. Acta 106 (2013) 418–424, https://doi.org/10.1016/j.electacta.2013.05.136.

[11] E. Achenbach, Three-dimensional and time-dependent simulation of a planar solid oxide fuel cell stack, J. Power Sources 49 (1994) 333–348, https://doi.org/10.1016/0378-7753(93)01833-4.

[12] K. Recknagle, R. Williford, L. Chick, D. Rector, M. Khaleel, Three-dimensional thermo-fluid electrochemical modeling of planar SOFC stacks, J. Power Sources 113 (2003) 109–114, https://doi.org/10.1016/S0378-7753(02)00487-1.

[13] R.T. Nishida, S.B. Beale, J.G. Pharoah, Comprehensive computational fluid dynamics model of solid oxide fuel cell stacks, Int. J. Hydrogen Energy 41 (2016) 20592–20605, https://doi.org/10.1016/j.ijhydene.2016.05.103.

[14] M. Andersson, H. Paradis, J. Yuan, B. Sundén, Three dimensional modeling of an solid oxide fuel cell coupling charge transfer phenomena with transport processes and heat generation, Electrochim. Acta 109 (2013) 881–893, https://doi.org/10.1016/j.electacta.2013.08.018.

[15] A. Leonide, V. Sonn, A. Weber, E. Ivers-Tiffée, Evaluation and modeling of the cell resistance in anode-supported solid oxide fuel cells, J. Electrochem. Soc. 155 (2008) B36–B41, https://doi.org/10.1149/1.2801372.

[16] A. Leonide, SOFC Modeling and Parameter Identification by Means of Impedance Spectroscopy, Dissertation, Institut für Werkstoffe der Elektrotechnik (IWE), Universitat Karlsruhe (TH), 2010.

[17] J. Joos, T. Carraro, A. Weber, E. Ivers-Tiffée, Reconstruction of porous electrodes by FIB/SEM for detailed microstructure modeling, J. Power Sources 196 (2011) 7302–7307, https://doi.org/10.1016/j.jpowsour.2010.10.006.

[18] J. Joos, M. Ender, I. Rotscholl, N.H. Menzler, E. Ivers-Tiffée, Quantification of double-layer Ni/YSZ fuel cell anodes from focused ion beam tomography data, J. Power Sources 246 (2014) 819–830, https://doi.org/10.1016/j.jpowsour.2013.08.021.

[19] A. Leonide, S. Hansmann, A. Weber, E. Ivers-Tiffée, Performance simulation of current/voltage-characteristics for SOFC single cell by means of detailed impedance analysis, J. Power Sources 196 (2011) 7343–7346, https://doi.org/10.1016/j.jpowsour.2010.10.052.

[20] J.-C. Njodzefon, D. Klotz, A. Kromp, A. Weber, E. Ivers-Tiffée, Electrochemical modeling of the current-voltage characteristics of an SOFC in fuel cell and electrolyzer operation modes, J. Electrochem. Soc. 160 (2013) F313–F323, https://doi.org/10.1149/2.018304jes.

[21] H. Timmermann, D. Fouquet, A. Weber, E. Ivers-Tiffée, U. Hennings, R. Reimert, Internal reforming of methane at Ni/YSZ and Ni/CGO SOFC cermet anodes, Fuel Cells 6 (2006) 307–313, https://doi.org/10.1002/fuce.200600002.

[22] H. Timmermann, W. Sawady, R. Reimert, E. Ivers-Tiffée, Kinetics of (reversible) internal reforming of methane in solid oxide fuel cells under stationary and APU conditions, J. Power Sources 195 (2010) 214–222, https://doi.org/10.1016/j.jpowsour.2009.07.019.

[23] N. Russner, H. Geisler, S. Dierickx, A. Weber, E. Ivers-Tiffée, A non-isothermal 2D stationary FEM model for hydrocarbon fueled SOFCs stack layers, ECS Trans 78 (2017) 2673–2682, https://doi.org/10.1149/07801.2673ecst.

[24] H. Geisler, A. Kromp, A. Weber, E. Ivers-Tiffée, Stationary FEM model for performance evaluation of planar solid oxide fuel cells connected by metal interconnectors, J. Electrochem. Soc. 161 (2014) F778–F788, https://doi.org/10.1149/2.079406jes.

[25] J. Spurk, N. Aksel, Stromungslehre, Springer-Verlag, Berlin, Heidelberg, 2019, https://doi.org/10.1007/978-3-662-58764-5.

[26] (Gvc) Verein Deutscher Ingenieure - Gesellschaft Verfahrenstechnik und Chemieingenieurwesen, VDI-warmeatlas, Springer-Verlag, Berlin, Heidelberg, 2006, https://doi.org/10.1007/978-3-540-32218-4.

[27] Christian Wedershoven, Transport Parameters of Thin, Supported Cathode Layers in Solid Oxide Fuel Cells (SOFCs), Forschungszentrum Jülich GmbH, Jülich, 2010.

[28] J. Joos, M. Ender, T. Carraro, A. Weber, E. Ivers-Tiffée, Representative volume element size for accurate solid oxide fuel cell cathode reconstructions from focused ion beam tomography data, Electrochim. Acta 82 (2012) 268–276, https://doi.org/10.1016/j.electacta.2012.04.133.

[29] N. Russner, D. Horny, J. Joos, E. Ivers-Tiffée, Mass and heat transport in porous SOFC electrodes, in: Proc. Thirteen. Int. Symp. Solid Oxide Fuel Cells, 2018, p. A1302.

[30] ThyssenKrupp, Crofer 22 APU - Material Data Sheet No. 4046, ThyssenKrupp VDM, 2010.

[31] N. Grigorev, K. Sick, N.H. Menzler, O. Guillon, R. Telle, Development of cathode contacting for SOFC stacks, in: Proc. Thirteen. Int. Symp. Solid Oxide Fuel Cells, 2018, p. B0902.

[32] S. Dierickx, T. Mundloch, A. Weber, E. Ivers-Tiffée, Advanced impedance model for double-layered solid oxide fuel cell cermet anodes, J. Power Sources 415 (2019) 69–82, https://doi.org/10.1016/j.jpowsour.2019.01.043.

[33] P.R. Shearing, D.J.L. Brett, N.P. Brandon, Towards intelligent engineering of SOFC electrodes: a review of advanced microstructural characterisation techniques, Int. Mater. Rev. 55 (2010) 347–363, https://doi.org/10.1179/095066010X12777205875679.

[34] S. Primdahl, Oxidation of hydrogen on Ni/Yttria-Stabilized zirconia cermet anodes, J. Electrochem. Soc. 144 (1997) 3409, https://doi.org/10.1149/1.1838026.

[35] S. Dierickx, J. Joos, A. Weber, E. Ivers-Tiffée, Advanced impedance modelling of Ni/8YSZ cermet anodes, Electrochim. Acta 265 (2018) 736–750, https://doi.org/10.1016/j.electacta.2017.12.029.

[36] V. Sonn, A. Leonide, E. Ivers-Tiffée, Combined deconvolution and CNLS fitting approach applied on the impedance response of technical Ni/8YSZ cermet electrodes, J. Electrochem. Soc. 155 (2008) B675, https://doi.org/10.1149/1.2908860.

[37] C. Endler-Schuck, J. Joos, C. Niedrig, A. Weber, E. Ivers-Tiffée, The chemical oxygen surface exchange and bulk diffusion coefficient determined by impedance spectroscopy of porous. $La_{0.58}Sr_{0.4}Co_{0.2}Fe_{0.8}O_{3-\delta}$ (LSCF) cathodes, Solid State Ion. 269 (2015) 67–79, https://doi.org/10.1016/j.ssi.2014.11.018.

[38] C. Breitkopf, K. Swider-Lyons, Handbook of Electrochemical Energy, Springer-Verlag, 2017, 9783662466575.

[39] A. Kromp, A. Leonide, A. Weber, E. Ivers-Tiffée, Electrochemical analysis of reformate-fuelled anode supported SOFC, J. Electrochem. Soc. 158 (2011) B980–B986, https://doi.org/10.1149/1.3597177.

[40] V.M. Janardhanan, O. Deutschmann, CFD analysis of a solid oxide fuel cell with internal reforming: coupled interactions of transport, heterogeneous catalysis and electrochemical processes, J. Power Sources 162 (2006) 1192–1202, https://doi.org/10.1016/j.jpowsour.2006.08.017.

[41] K. Nikooyeh, A.A. Jeje, J.M. Hill, 3D modeling of anode-supported planar SOFC with internal reforming of methane, J. Power Sources 171 (2007) 601–609, https://doi.org/10.1016/j.jpowsour.2007.07.003.

[42] R. Krishna, J.A. Wesselingh, The Maxwell-Stefan approach to mass transfer 52 (1997) 861–911.

[43] S. Chapman, T.G. Cowling, D. Burnett, The Mathematical Theory of Non-uniform Gases: an Account of the Kinetic Theory of Viscosity, Thermal Conduction and Diffusion in Gases, third ed., Cambridge University Press, 1990.

[44] E.A. Mason, A.P. Malinauskas, R.B. Evans, Flow and diffusion of gases in porous media, J. Chem. Phys. 46 (1967) 3199–3216, https://doi.org/10.1063/1.1841191.

[45] H. Zhu, R.J. Kee, V.M. Janardhanan, O. Deutschmann, D.G. Goodwin, Modeling elementary heterogeneous chemistry and electrochemistry in solid-oxide fuel cells, J. Electrochem. Soc. 152 (2005) A2427–A2440, https://doi.org/10.1149/1.2116607.

[46] L. Petruzzi, S. Cocchi, F. Fineschi, A global thermo-electrochemical model for SOFC systems design and engineering, J. Power Sources 118 (2003) 96–107, https://doi.org/10.1016/S0378-7753(03)00067-3.

[47] S. Campanari, P. Iora, Definition and sensitivity analysis of a finite volume SOFC model for a tubular cell geometry, J. Power Sources 132 (2004) 113–126, https://doi.org/10.1016/j.jpowsour.2004.01.043.

[48] P. Costamagna, A. Selimovic, M. Del Borghi, G. Agnew, Electrochemical model of the integrated planar solid oxide fuel cell (IP-SOFC), Chem. Eng. J. 102 (2004) 61–69, https://doi.org/10.1016/j.cej.2004.02.005.

[49] B.A. Haberman, J.B. Young, A detailed three-dimensional simulation of an IP-SOFC stack, J. Fuel Cell Sci. Technol. 5 (2008), 011006, https://doi.org/10.1115/1.2786468.

[50] W. Lehnert, J. Meusinger, F. Thom, Modelling of gas transport phenomena in SOFC anodes, J. Power Sources 87 (2000) 57–63, https://doi.org/10.1016/S0378-7753(99)00356-0.

[51] H. Yokokawa, S. Yamauchi, T. Matsumoto, Thermodynamic database MALT for Windows with gem and CHD, Calphad 26 (2002) 155–166, https://doi.org/10.1016/S0364-5916(02)00032-9.

[52] D.L. Damm, A.G. Fedorov, Radiation heat transfer in SOFC materials and components, J. Power Sources 143 (2005) 158–165, https://doi.org/10.1016/j.jpowsour.2004.11.063.

[53] W.M. Rohsenow, J.P. Hartnett, Y.I. Cho, Handbook of Heat Transfer, McGraw-Hill, New York, 1998.

[54] J.K. Carson, S.J. Lovatt, D.J. Tanner, A.C. Cleland, Thermal conductivity bounds for isotropic, porous materials, Int. J. Heat Mass Transf. 48 (2005) 2150–2158, https://doi.org/10.1016/j.ijheatmasstransfer.2004.12.032.

[55] T. Kawashima, M. Hishinuma, Thermal properties of porous Ni/YSZ particulate composites at high temperatures, Mater. Trans., JIM 37 (1996) 1518–1524, https://doi.org/10.2320/matertrans1989.37.1518.

[56] R.W. Powell, R.P. Tye, M.J. Hickman, The thermal conductivity of nickel, Int. J. Heat Mass Transf. 8 (1965) 679–688, https://doi.org/10.1016/0017-9310(65)90017-7.

[57] K.W. Schlichting, N.P. Padture, P.G. Klemens, Thermal conductivity of dense and porous yttria-stabilized zirconia, J. Mater. Sci. 36 (2001) 3003–3010, https://doi.org/10.1023/A:1017970924312.

[58] Y.-C. Shin, S. -i. Hashimoto, K. Yashiro, K. Amezawa, T. Kawada, Thermal properties of perovskite-type oxides $La_{0.6}Sr_{0.4}Co_{1-X}Fe_xO_{3-\delta}$ ($0 < x < 1.0$), ECS Trans 72 (2016) 105–110, https://doi.org/10.1149/07207.0105ecst.

[59] J.G. Hemrick, C.W. Kistler, A.A. Wereszczak, M.K. Ferber, Thermal conductivity of alumina measured with three techniques, J. Test. Eval. 31 (2003) 11622, https://doi.org/10.1520/JTE12368J.

[60] K.J. Daun, S.B. Beale, F. Liu, G.J. Smallwood, Radiation heat transfer in planar SOFC electrolytes, J. Power Sources 157 (2006) 302–310, https://doi.org/10.1016/j.jpowsour.2005.07.045.

[61] K. Kanamura, Dependence of entropy change of single electrodes on partial pressure in solid oxide fuel cells, J. Electrochem. Soc. 138 (1991) 2165–2167, https://doi.org/10.1149/1.2085944.

[62] Z. Takehara, K. Kanamura, S. Yoshioka, Thermal energy generated by entropy change in solid oxide fuel cell, J. Electrochem. Soc. 136 (1989) 2506–2511, https://doi.org/10.1149/1.2097448.

[63] P. Stephan, K. Schaber, K. Stephan, F. Mayinger, Thermodynamik, 2013, https://doi.org/10.1007/978-3-642-30098-1.

[64] J. Francl, W.D. Kingery, Thermal conductivity: IX, experimental investigation of effect of porosity on thermal conductivity, J. Am. Ceram. Soc. 37 (1954) 99–107, https://doi.org/10.1111/j.1551-2916.1954.tb20108.x.

[65] M. Kornely, A. Leonide, A. Weber, E. Ivers-Tiffée, Performance limiting factors in anode-supported cells originating from metallic interconnector design, J. Power Sources 196 (2011) 7209–7216, https://doi.org/10.1016/j.jpowsour.2010.10.048.

[66] L. Blum, P. Batfalsky, Q. Fang, L.G.J. de Haart, J. Malzbender, N. Margaritis, N. H. Menzler, R. Peters, SOFC stack and system development at Forschungszentrum Jülich, J. Electrochem. Soc. 162 (2015) F1199–F1205, https://doi.org/10.1149/2.0491510jes.

[67] Q. Fang, L. Blum, R. Peters, M. Peksen, P. Batfalsky, D. Stolten, SOFC stack performance under high fuel utilization, Int. J. Hydrogen Energy 40 (2015) 1128–1136, https://doi.org/10.1016/j.ijhydene.2014.11.094.

[68] Q. Fang, L. Blum, P. Batfalsky, N.H. Menzler, U. Packbier, D. Stolten, Durability test and degradation behavior of a 2.5 kW SOFC stack with internal reforming of LNG, Int. J. Hydrogen Energy 38 (2013) 16344–16353, https://doi.org/10.1016/j.ijhydene.2013.09.140.

[69] B. Rietveld, SOFC Stack Polarisation Curve with POX or ATR Diesel, 2006, pp. 1–8.

[70] D. Klotz, A. Weber, E. Ivers-Tiffée, Practical guidelines for reliable electrochemical characterization of solid oxide fuel cells, Electrochim. Acta 227 (2017) 110–126, https://doi.org/10.1016/j.electacta.2016.12.148.